Millimeter Wave Imaging and Phased Array Antennas for 5G and Aerospace Applications

Helander, Jakob

2019

Document Version:
Publisher's PDF, also known as Version of record

Millimeter Wave Imaging and Phased Array Antennas for 5G and Aerospace Applications

Jakob Helander

Doctoral Dissertation
Electromagnetic Theory

Lund University
Lund, Sweden
2019

Doctoral dissertation which, by due permission of the Faculty of Engineering, Lund University, will be publicly defended on March 26, 2019, at 9:15 a.m. in lecture hall E:C, John Ericssons väg 4, Lund, for the degree of Doctor of Philosophy in Engineering in Electromagnetic Theory.

Department of Electrical and Information Technology
Electromagnetic Theory Group
Lund University
P.O. Box 118, S-221 00 Lund, Sweden

Series of licentiate and doctoral theses
ISSN 1654-790X; No. 119
ISBN 978-91-7753-924-7 (print)
ISBN 978-91-7753-925-4 (digital)

Typeset in Computer Modern 10 pt using LaTeX and BibTeX.
Printed in Sweden by *Tryckeriet i E-huset*, Lund University, Lund.
February, 2019

To whom it may concern...

Abstract

Phased array antennas are cornerstones in many proposed antenna solutions concerning the next generation of both airborne radar systems and wireless communication systems (5G). Additionally, millimeter wave (mm-wave) frequencies are expected to play an integral role in 5G, and are deemed well-suited for inspecting structural components used in the aerospace industry.

This dissertation consists of a general introduction (Part I) and six scientific papers (Part II)—of which four have been published and two are under review in peer-reviewed international journals. The introduction comprises the background, the motivation and the subject-specific technical foundation on which the research presented in the included papers is based on. Fundamental theory on antenna arrays, mm-wave imaging systems and computational electromagnetics are presented together with the specific performance metrics, experimental setups, and computational acceleration algorithms that are of interest for the contained research work. The included papers can be divided into three tracks with two distinct applicational overlaps.

Papers I and II concern electrically large phased arrays for airborne systems, and the numerical techniques that alleviate time-efficient and accurate simulations of such antennas. Paper I investigates the performance of two different approaches to the macro basis function (MBF) method for interconnected subdomains under the harsh electromagnetic conditions that endfire operation implies. Paper II presents a synthesis technique for endfire operation of large scale arrays that utilizes convex optimization to improve the impedance matching performance. A hybridized method of moments (MoM) comprising the MBF method, the adaptive cross approximation (ACA) and a translational symmetry scheme, enables swift and accurate simulations of the electrically large geometry.

Papers III and IV concern phased arrays—integrated in the user equipment (UE) and operating at mm-wave frequencies—for 5G applications. In Paper III, various array configurations of two microstrip antenna designs are evaluated with respect to two radiation performance metrics introduced specifically for evaluating the beam steering capabilities of phased array systems in the UE. A novel near field measurement technique for running electromagnetic field (EMF) exposure compliance tests of mm-wave phased arrays for future 5G devices is presented in Paper IV. Measurement data is retrieved using a planar scan, and probe correction is realized through an additional measurement of a small aperture.

Papers V and VI deal with mm-wave imaging systems developed for nondestructive testing (NDT) of composite materials used in the aerospace industry. A transmission-based bistatic imaging system is presented in Paper V, whereas Paper VI presents a further development of this system in a reflection-based measurement scenario. Data is retrieved using a planar scan, and the image retrieval algorithms comprise a numerical technique to separate the sources that contribute to the measured data, and an L_1-minimization formulation to exploit potential sparsity of the sought-after solution.

Populärvetenskaplig sammanfattning

En fasstyrd gruppantenn är en konfiguration av flera antennelement som tillsammans agerar som en enkel antenn, och genom att kontrollera matningsfasen till samtliga element kan ett adaptivt strålningsmönster realiseras så att huvudloben styrs elektriskt i en önskad riktning. Elektriskt storskaliga konfigurationer av denna typ—innehållande flera hundratals eller tusentals antennelement—används i moderna luftburna radarsystem, huvudsakligen på grund av att en mycket hög riktverkan—som uppstår som en konsekvens av det mycket stora antalet antennelement—är nödvändig samtidigt som själva huvudloben måste kunna styras för att manövrera radarn i en större rumslig region.

Fasstyrda gruppantenner har också varit ett fokusområde som en potentiell antennlösning för handhållna användarenheter som ska vara funktionsdugliga i 5:e generationens trådlösa system (5G). För att tillgodose de kapacitetskrav som ställs på de framtida 5G-näten har millimetervågsfrekvensbanden—de band där motsvarande våglängder sträcker sig mellan 1 mm och 10 mm—framställts som en av de mest populära lösningarna, just eftersom det där finns en enorma bandbredd att exploatera. I sin tur möjliggör det att gruppantenner kan integreras i handhållna enheter, eftersom antennelementen i sig kan designas i storleksordningen av en halv våglängd eller mindre.

Millimetervågor har också användningsområden inom flygindustrin, där till exempel avbildningssystem verkande i dessa frekvensband kan utnyttjas för att genomföra oförstörande provning (OFP) av olika kompositstrukturer som ofta utgör en viktig del av flygplanskroppen. Kompositstrukturer, som är sammansättningar av olika material, används till exempel för att förverkliga specifika elektromagnetiska egenskaper, och det är därför viktigt att försäkra sig om att varje enskilt producerad enhet ej innehåller felaktigheter i form av till exempel delamineringar eller inhomogeniteter. I detta syfte kan ett millimetervågsavbildningssystem för OFP användas för att karakterisera ett provs elektromagnetiska egenskaper, utan att för den delen äventyra själva kompositionen av provet. Ett system som opererar i millimetervågsfrekvensområdet introducerar en fördel i förbättrad upplösning, samt möjliggör en mer kompakt mätuppställning vilket är, ur en praktisk synvinkel, fördelaktigt under en akademisk utvecklingsfas.

I denna avhandling berörs de tre ovanstående tillämpningsområdena via ett antal olika forskningsprojekt med diverse ändamål. Först berörs den så kallade ”endfire” excitationen av en fasstyrd gruppantenn bestående av tusentals antennelement. Detta driftsätt ger upphov till en kritisk elektromagnetisk miljö, och för att erhålla simuleringsdata med hög noggrannhet på ett tidseffektivt sätt ställs specifika krav på de applicerbara numeriska beräkningsmetoderna. Vidare studeras design, funktionsduglighet och begränsningar av millimetervågsgruppantenner för 5G-applikationer. Slutligen presenteras varianter av ett avbildningssystem, utvecklat i OFP-syfte och verkande på millimetervågsfrekvenser, bestående av både experimentell mätuppställning och framtagen mjukvara.

Preface

This thesis summarizes the research that I have carried out at the Department of Electrical and Information Technology, Lund University, Sweden. The research has been conducted within the framework of several industrially launched projects. The thesis starts with a research overview followed by the scientific papers as listed below. The order is not chronological, but chosen as to clearly depict the common denominators of the various papers.

List of Included Papers

I. J. Helander, D. Tayli, and D. Sjöberg, "A Comparison of Macro Basis Function Methods for Interconnected Endfire Antenna Arrays," *IEEE Antennas and Wireless Propagation Letters*, Vol. 16, pp. 2159–2162, 2017.

Contributions of the author: The author of this thesis performed the full comparison study of the two methods and wrote the majority of the paper.

II. J. Helander, D. Tayli, and D. Sjöberg, "Synthesis of Large Endfire Antenna Arrays using Convex Optimization," *IEEE Transactions on Antennas and Propagation*, Vol. 66, No. 2, pp. 712–720, 2018.

Contributions of the author: The author of this thesis ran all simulations, did the analysis of the data, and wrote the majority of the paper. The main simulation software was written by Doruk Tayli, with whom the author co-implemented the compression and acceleration algorithms.

III. J. Helander, K. Zhao, Z. Ying, and D. Sjöberg, "Performance Analysis of Millimeter Wave Phased Array Antennas in Cellular Handsets," *IEEE Antennas and Wireless Propagation Letters*, Vol. 15, pp. 504–507, 2016.

Contributions of the author: The author of this thesis ran all simulations, did the analysis of the data, and wrote the majority of the paper. The author co-designed the antennas together with Zhinong Ying, who also conceived the idea. The measurements were conducted by Kun Zhao and Zhinong Ying.

IV. J. Lundgren, J. Helander, M. Gustafsson, D. Sjöberg, B. Xu, and D. Colombi, "Near Field Measurement and Calibration Technique for Compliance Testing of mm-wave 5G Devices," *Scientific Reports*, 2019, submitted.[1]

Contributions of the author: The author of this thesis co-designed the experimental setup and conducted the measurements together with Johan Lundgren. The author performed a smaller part of the data processing,

[1] 3rd place Student Paper Award at the AMTA 2018 Conference in Williamsburg, VA.

developed some of the features of the simulation code, and wrote parts of the paper. Johan Lundgren performed the majority of the data processing, and wrote the majority of the paper.

V. J. Helander, A. Ericsson, M. Gustafsson, T. Martin, D. Sjöberg and C. Larsson, "Compressive Sensing Techniques for mm-wave Non-Destructive Testing of Composite Panels," *IEEE Transactions on Antennas and Propagation*, Vol. 65, No. 10, pp. 5523–5531, 2017.

Contributions of the author: The author of this thesis co-designed the experimental setup and conducted the measurements together with Andreas Ericsson. The author performed all post processing of the measurement data and wrote the majority of the paper.

VI. J. Helander, J. Lundgren, D. Sjöberg, C. Larsson, T. Martin, and M. Gustafsson, "Reflection-Based Inverse Scattering for Sparse Image Reconstruction," *IEEE Transactions on Antennas and Propagation*, 2018, submitted.[2]

Contributions of the author: The author of this thesis designed the experimental setup, implemented and performed all post processing routines, and wrote the majority of the paper. The measurements were conducted together with Johan Lundgren.

Other Publications by the Author

The author of this dissertation is also the author or co-author of the following publications which are related to but not considered part of the dissertation:

VII. K. Zhao, J. Helander, D. Sjöberg, S. He, T. Bolin, and Z. Ying, "User Body Effect on Phased Array in User Equipment for 5G mm-wave Communication System," *IEEE Antennas and Wireless Propagation Letters*, Vol. 16, pp. 864–867, 2017.

VIII. G. Wolgast, C. Ehrenborg, A. Israelsson, J. Helander, E. Johansson, and H. Månefjord, "Wireless Body Area Network for Heart Attack Detection [Education Corner]," *IEEE Antennas and Propagation Magazine*, Vol. 58, No. 5, pp. 84–92, 2016.

IX. J. Helander, D. Sjöberg, and D. Tayli, "On the Issue of Simulating Very Large Endfire Arrays with Complex Antenna Geometries," *URSI International Symposium on Electromagnetic Theory (EMTS)*, Espoo, Finland, 2016.

[2] 1st place Student Paper Award at the AMTA 2018 Conference in Williamsburg, VA.

X. Z. Ying, K. Zhao, T. Bolin, J. Helander, , D. Sjöberg, S. He, A. Scannavini, L. J. Foged, and G. Nicolas, "Study of Phased Array in UE for 5G mm-wave Communication System with Consideration of User Body Effect," *10th European Conference on Antennas and Propagation (EuCAP)*, Davos, Switzerland, 2016.

XI. J. Helander, A. Ericsson, D. Sjöberg, M. Gustafsson, T. Martin, and C. Larsson, "60 GHz Imaging of Panels for Defect Detection using Planar Scanning," *IEEE International Symposium on Antennas and Propagation (APS URSI)*, Fajardo, Puerto Rico, 2016.

XII. B. Xu, J. Helander, A. Ericsson, Z. Ying, S. He, M. Gustafsson, and D. Sjöberg, "Investigation of Planar Near Field Measurement of Millimeter Wave Antenna for 5G Application," *International Symposium on Antennas and Propagation (ISAP)*, Okinawa, Japan, 2016.

XIII. K. Zhao, J. Helander, Z. Ying, D. Sjöberg, M. Gustafsson, and S. He, "mm-wave Phased Array in Mobile Terminal for 5G Mobile System with Consideration of Hand Effect," *IEEE Vehicular Technology Conference (VTC)*, Glasgow, United Kingdom, 2015.

XIV. J. Helander, D. Sjöberg, M. Gustafsson, K. Zhao, and Z. Ying, "Characterization of mm-wave Phased Array Antennas in Mobile Terminal for 5G Mobile System," *IEEE International Symposium on Antennas and Propagation (APS URSI)*, Vancouver, Canada, 2015.

Acknowledgments

First of all, I would like to thank my main supervisor Prof. Daniel Sjöberg. Despite taking on the huge responsibility of becoming Head of Department as I joined the research group, you wholeheartedly devoted yourself to help and guide me in the research process. Your passion for science, and your encouraging and positive mindset are truly inspiring.

I would also like to thank my co-supervisors Prof. Mats Gustafsson, Dr. Torleif Martin and Prof. Christer Larsson. Mats, you are a true role model, and your devotion to support and motivate me as an aspiring young researcher does not go unnoticed; thank you. Torleif and Christer, I highly value your support and guidance, and the industrial perspective on my research that you have given me.

Literally all of my current and former colleagues should also be acknowledged. I have had the pleasure to meet, work with, and get to know many skillful PhD students over the course of my studies: Dr. Mikael Henriksson, Dr. Andreas Ericsson, Dr. Doruk Tayli, Niklas Ivarsson, Casimir Ehrenborg, Johan Lundgren, Christian Nelson, Dr. Kun Zhao, Dr. Bo Xu, and many more that I forgot to mention here by name. Among the seniors, Prof. Gerhard Kristensson and Prof. Anders Karlsson have both contributed to an intellectually inspiring work environment and I am very thankful for their open-heartedness and support.

Under no circumstances may the people behind the industrial collaborations be forgotten. I am grateful to Anders Höök, Glenn Sjöberg and Kent Falk at Saab Electronic Defence Systems, Erik Abenius, Bo Strand and Emil Kieri at ESI Group, and Zhinong Ying at Sony Mobile Communications, for sharing their knowledge and expertise during the time frame of the respective projects.

Naturally, I would like to thank the Swedish Governmental Agency for Innovation Systems (VINNOVA), the National Aeronautics Research Programme (NFFP), the Swedish Defence Materiel Administration (FMV), the Swedish Foundation for Strategic Research (SSF), and the Swedish Armed Forces for funding a large fraction of this thesis work. Also, many thanks to the institutes and foundations—the Royal Physiographic Society of Lund, the LM Ericsson Research Foundation, Ernold Lundströms Stiftelse, Skånska Ingenjörsklubben, the Japan Society for Promotion of Science (JSPS), and the Swedish Foundation for International Cooperation in Research and Higher Education (STINT)—that granted me a number of scholarships that made attendance at conferences and my research visit to Tokyo Institute of Technology possible. Furthermore, I express my gratitude to Prof. Jiro Hirokawa and Prof. Takashi Tomura for hosting me during my Japan visit.

And last but not least, many thanks to the people in my private life who offered support and comfort when I needed it the most. You know who you are.

Lund, February 2019
Jakob Helander

Acronyms and Abbreviations

3D	three-dimensional
5G	fifth generation wireless communication networks
AESA	active electronically scanned array
ACA	adaptive cross approximation
ARC	active reflection coefficient
AUT	antenna under test
BPDN	basis pursuit denoise
CEM	computational electromagnetics
CS	compressive sensing
DoFs	degrees of freedom
DUT	device under test
EEP	embedded element pattern
EFIE	electric field integral equation
EM	electromagnetic
EMF	electromagnetic field
FFT	fast Fourier transform
H-W	Hansen-Woodyard
LOS	line-of-sight
MBF	macro basis function
MIMO	multiple input multiple output
MLFMM	multilevel fast multipole method
mm-wave	millimeter wave
MoM	method of moments
NDT	non-destructive testing
NLOS	non-line-of-sight
PEC	perfect electric conductor
PESA	passive electronically scanned array

RCS	radar cross section
RF	radio frequency
RRE	radar range equation
RWG	Rao-Wilton-Glisson
Rx	receive
SNR	signal-to-noise ratio
SVD	singular value decomposition
TARC	total active reflection coefficient
TE	transverse electric
TM	transverse magnetic
Tx	transmit
T/R	transmit and receive
UE	user equipment
VNA	vector network analyzer

Contents

Part I: Introduction and Research Overview

Jakob Helander

1 Background and Motivation

Large scale phased array antennas are utilized in many of the deployed airborne radar systems that are in use today. The narrow, high gain radiated beam that is generated by the large number of antenna elements can be electronically steered through variable control of the phase between each element, thus realizing a flexible scan strategy to rapidly perform, *e.g.*, the search and track task at hand [1]. The mature and well-established passive electronically scanned array (PESA) technology is the most common solution in use, where a single transmit and receive (T/R) module feeds the array and a separate phase shifter is connected to each antenna. Due to the continuously increasing operational requirements and recent advancements in reducing the cost and weight of the underlying radio frequency (RF) subsystems however, the more advanced active electronically scanned array (AESA) technology—exploiting a much larger number of T/R modules—is rapidly maturing and provides further benefits in terms of enhanced scan flexibility and adaptive beam pattern control, and more efficient use of the radiated energy [2, 3].

Some examples of airborne AESA radars are shown in Figure 1, with simulation models taken from the commercial simulation software ESI CEM One [4]. The antenna element typically incorporates a high degree of material complexity and design detail, making it computationally cumbersome to simulate an array configuration consisting of several hundreds or thousands of elements as an extremely large number of unknowns is necessary for sufficient numerical accuracy. For instance, the element shown to the bottom left in Figure 1, although simplified, still comprises several dielectric materials and electrically small conducting details, resulting in a large number of unknowns only for the single antenna element. Accordingly, approximative acceleration methods are necessary to simulate the exceedingly large electromagnetic (EM) problem of the full array. Moreover, if one wants to push the forefront of the AESA functionality in terms of array design and synthesis—*e.g.*, by investigating the mutual coupling effects during endfire mode operation of the array—it is paramount to utilize any *a priori* information at hand to properly select the hybrid numerical solver.

In addition to the aforementioned airborne applications, phased arrays are extensively utilized in different formats in a large variety of other modern applications such as automotive radar, various space applications, and telecommunications to name a few. For instance, phased array technology constitutes a cornerstone of the extensively researched millimeter wave (mm-wave) (30–300 GHz) communication systems that have emerged as disruptive innovations for the future 5:th generation (5G) wireless communication networks [5–7]. The move towards the mm-wave frequency bands can largely be explained by the saturated spectrum in the conventional bands below 6 GHz, and the increasing demands on capacity that is a result of technological advances and the development of new use cases (*e.g.*, low latency streaming of high definition videos on a smartphone). Evidently, exploiting the large, underutilized mm-wave spectrum implies

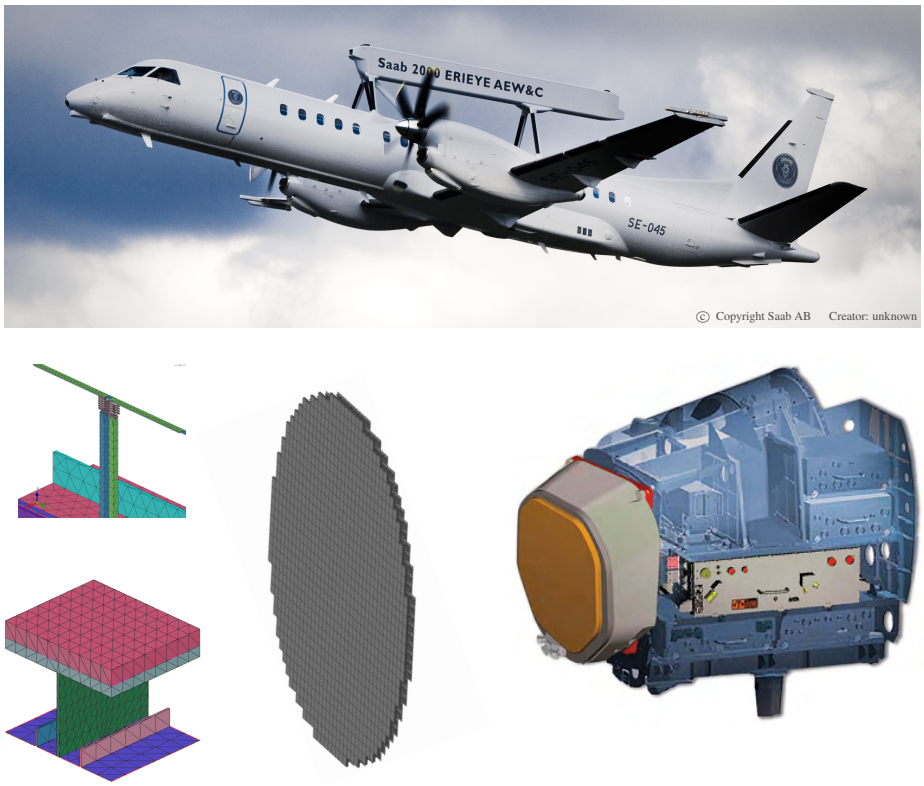

Figure 1: Example of AESA radars. Top: A Saab 2000 Erieye AEW&C aircraft with the AESA radar mounted on the fuselage © Saab AB. Bottom (left to right): Mesh view examples of a simplified antenna element for AESAs, simulation model example of nose cone AESA radar, and the AN-APG-63(V)3 nose cone AESA radar. The simulation models are taken from the commercial simulation software ESI CEM One [4].

that a substantial increase in channel capacity is possible, enabling the users to experience several gigabits-per-second data rates.

One of the prerequisites for realizing mm-wave communication systems is the utilization of phased arrays in the user equipment (UE) [8–10]. The much higher gain achievable using phased array configurations aims at mitigating the increased signal attenuation that arises due to, *e.g.*, additional path loss, precipitation effects, and higher signal sensitivity to blockage effects in the propagation environment [6, 11, 12]. Furthermore, precise phase control permits the narrow, high gain beam to be steered in order to expand the otherwise very limited spatial coverage. Since the dimensions of resonant type antennas decrease with increasing frequency, it becomes possible to integrate mm-wave phased arrays in the limited physical space that commercial UEs constitute. The antenna element's

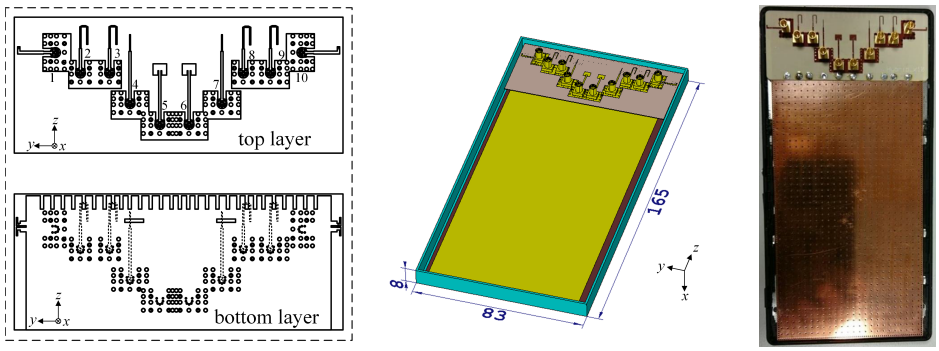

Figure 2: Example of a UE-integrated 28 GHz phased array configuration designed for 5G applications [8] © 2018 IEEE. The ten element array comprises several sub array configurations. From left to right: Close-up view, simulation model with back cover removed, and fabricated mock-up.

largest dimension L is roughly half the effective wavelength:

$$L \approx \frac{\lambda_{\text{eff}}}{2} = \frac{c}{2f\sqrt{\varepsilon_{\text{eff}}}}\,, \tag{1.1}$$

where c is the speed of light in vacuum, f is the frequency, and ε_{eff} is the effective permittivity of the medium surrounding the antenna. For instance, $L \approx 2.5\,\text{mm}$ for an antenna resonant at 28 GHz embedded in the printed circuit board material FR-4 (dielectric constant of 4.4). Figure 2 shows an example of a UE-integrated 28 GHz phased array configuration for 5G applications.

Yet, despite the relatively straightforward antenna-related technological adaptions necessary for realizing mm-wave communication systems on a commercial scale, there are still many non-trivial challenges that need to be addressed concerning the utilization of phased arrays in UEs of limited form factors. Many of these are related to constraints on both hardware and architecture of the underlying mm-wave systems that need to provide low loss and compact solutions while continuously ensuring high data rate link accessibility (*e.g.*, reliable beam forming architecture, and adaptive array processing algorithms) [7, 13–15]. Other, more antenna-related concerns are, *e.g.*, distortion effects on the radiation pattern, realizing polarization diversity and omnidirectional coverage, and ensuring compliance with regulatory requirements on electromagnetic field (EMF) exposure [8, 16–19].

A mm-wave imaging system can for instance be used to conduct the necessary measurements for EMF exposure assessment, and further to visualize the sought-after quantities in a predetermined region around the antenna under test (AUT). Imaging in the mm-wave spectrum also finds its use in a wide range of other applications such as non-destructive testing (NDT), material characterization, antenna diagnostics, and medical screening [20, 21]. The first three of these are definitive examples of inverse source or inverse scattering problems in the EM

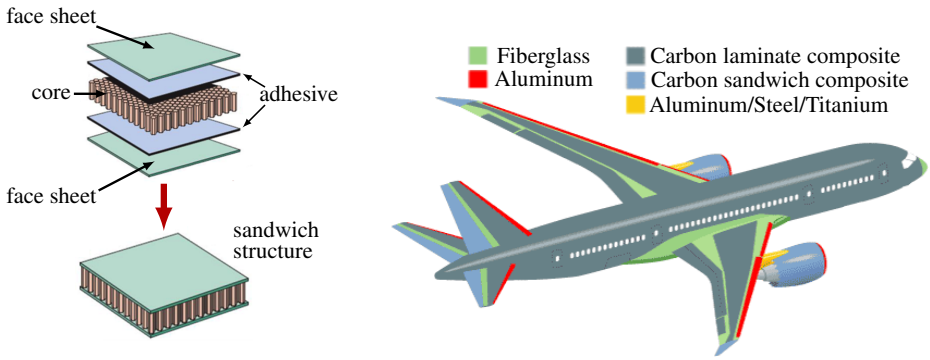

Figure 3: Example of composite structures utilized in the aerospace industry. Left: Laminated composite structure with a honeycomb core (adapted from [25]). Right: Usage of various composites and materials in the fuselage of a Boeing 787 (adapted from [26]).

domain [22]. In particular for NDT purposes, mm-wave imaging offers some beneficial characteristics as it has proven useful for detection of, *e.g.*, delaminations, material inhomogeneities, inclusions in low loss dielectrics, and cracks in metal surfaces and composite laminates [23]. As such, there are obvious applicabilities of mm-wave imaging in the aerospace and defense industry, as composite structures—that are subject to such anomalies and defects—are utilized here to a wide extent to reduce the overall weight, and realize the desired thermoelastic, mechanical and EM properties of, *e.g.*, the fuselage and wings of an aircraft [24–26]. An example of aerospace structural components and their usage in the aircraft fuselage is shown in Figure 3.

The main performance metrics of an imaging system are often taken as the achievable spatial resolution and dynamic range, as well as the overall measurement time necessary to acquire the sample data. Hence, to push the forefront of mm-wave imaging techniques, it is of great significance to treat the hardware and software components of the system both mutually and separately. Innovative experimental setups—as well as more classical ways to address the measurement—can be exploited jointly with state-of-the-art algorithm tools, *e.g.*, compressive sensing (CS) techniques, to come up with novel *ad hoc* strategies to well-specified EM problems.

Part I Structure

Section 2 gives a brief theoretical overview of the fundamental concepts of phased arrays, and introduces some of the more application specific metrics important for the work presented in this thesis. Then, Section 3 introduces the complete mm-wave imaging system—referring both to the hardware and software components—that constitutes a principal part of the research work contained in

this thesis. The experimental setup has been utilized to sample field data over a rectangular measurement surface, and various processing algorithms have been developed for the specific end applications of conducting NDT of composite panels and studying EMF exposure compliance of mm-wave antenna arrays. Section 4 introduces the fundamental concepts behind the method of moments (MoM) and presents the specific hybrid techniques that have been implemented, utilized and investigated under the scope of the research contained in this thesis. These techniques have been implemented as add-ons to an existing in-house MoM code [27] to obtain a hybridized solver that is particularly efficient in solving the problem of electrically large, finite sized antenna arrays. Finally, Section 5 concludes Part I with a summary of the research outcomes of the included papers and a research outlook.

2 Phased Arrays—An Overview

An antenna array is a group of single antenna elements that are configured such that they act as a single antenna [28]. Array configurations enable a higher maximum gain (beam forming) than what is realizable with only the single antenna element, and, furthermore, may permit the main beam to be steered by controlling the phase of each element (beam steering). Other useful properties and techniques that are realizable due to the increased complexity of the system are, *e.g.*, spatial diversity to increase capacity or reliability of a wireless channel, and spatial multiplexing for transmission of independently encoded data signals; two techniques that play integral roles in modern multiple input multiple output (MIMO) technologies [29, 30].

As antenna arrays are relevant in a wide range of applications, the form and size of the array, as well as the arrangement of the underlying electronics, might vary extensively depending on its intended use. For instance, the aforementioned active electronically scanned array (AESA) configuration typically consists of a large number of antenna elements where each element has its own T/R module. This enables high gain, electrical beam steering and adaptive pattern control through precise control of the phase and amplitude of the signal at each element. Similar concepts are also the target of extensive research concerning antenna arrays for 5G UE operating in the mm-wave frequency bands [8–10, 15, 18].

2.1 Phased Arrays in Radar and Communication

The necessity of utilizing antenna arrays in modern radar and future communication systems can be understood from the corresponding link budget formulas that estimate the overall gains and losses in the channel between the transmitting and receiving system. In monostatic radar applications, see Figure 4, the channel

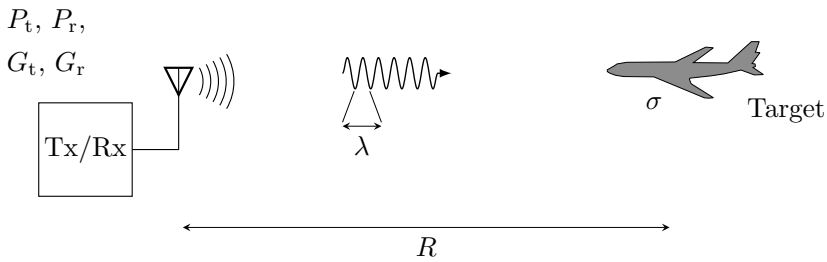

Figure 4: Monostatic radar-target scenario as described by the radar range equation in (2.1).

link budget is represented by the basic radar range equation (RRE) [31]:

$$P_r = \frac{P_t G_t G_r \lambda^2 \sigma}{(4\pi)^3 R^4 L_s} . \tag{2.1}$$

Here, P_r and P_t are the received and transmitted power, respectively, G_t and G_r are the far field gain of the antenna under transmit and receive, respectively, σ is the mean radar cross section (RCS) of the target, and R is the distance between the antenna and the target. System losses, *e.g.*, the atmospheric loss, are incorporated in the L_s-term. The operational wavelength λ is defined in terms of the speed of light c in the medium and the frequency f as $\lambda = c/f$.

Similarly, the Friis' transmission equation [32] provides the foundational formula for the link budget in communication systems:

$$P_r = \frac{P_t G_t G_r \lambda^2}{(4\pi R)^2 L_s} , \tag{2.2}$$

where R now is defined as the distance between the transmitting and receiving system. The term $(4\pi R)^2/\lambda^2$, referred to as the free space path loss, expresses a loss value that increases with decreasing wavelength and increasing distance. Both (2.1) and (2.2) are suitable representations of the link budget when R is a far field distance.

The far field region is defined as the region of the field of an antenna where the angular field distribution essentially is independent of the distance from a specified point in the antenna's region [33]. Any far field quantity is therefore a function of the spherical polar angle and azimuthal angle denoted θ and ϕ, respectively. The angular dependence of the far field characteristic is furthermore referred to as the antenna's radiation pattern [33]. For instance, the gain of an antenna in the far field region is defined as the ratio of the radiation intensity $U(\theta, \phi)$ (measured in units of W/sr) to the radiation intensity that would be produced if the power accepted by the antenna, P_{acc}, was isotropically radiated, *i.e.*,

$$G(\theta, \phi) = \frac{U(\theta, \phi)}{P_{acc}/4\pi} . \tag{2.3}$$

Moreover, the maximum gain of an antenna is related to its effective aperture, A_{e}, as:

$$G = \frac{4\pi A_{\mathrm{e}}}{\lambda^2}\,. \tag{2.4}$$

For antennas that are large compared to wavelength, A_{e} is closely related to the actual physical aperture size (which is not necessarily true for small antennas). Hence, (2.4) provides an intuition into the relation between maximum gain and the physical dimensions of, *e.g.*, a large array.

The directivity, $D(\theta, \phi)$, of an antenna is closely related to the gain, and ratios the radiation intensity with the radiated power, P_{rad}, instead of P_{acc}. As such, it is common to speak about an antenna's maximum directivity, *i.e.*, its ability to focus radiated power in the desired direction. This implies a more narrow beam for a larger value of maximum directivity (or gain); hence the term "beam forming".

It can be understood from the simple expressions in (2.1) and (2.2) that high gain is paramount to account for losses due to large R and/or small λ if the system already is specified in terms of transmitted power and minimum acceptable received power. As evident from (2.4), the introduction of the array configuration implies increased gain as the physical aperture increases. As disclosed in Section 1, the development of the AESA technology for large arrays in airborne radar systems is growing at a rapid pace; mainly due to its substantial advantages compared to mechanical steering of large aperture antennas in terms of lesser bulk and pace, and enhanced operational flexibility compared to the PESA technology [2, 3, 31]. In communication systems where beam forming is utilized in the UE to achieve high gain, it is imperative to exploit electrical beam steering to ensure that a link is realizable in the dynamic environment [6, 8, 9].

2.2 Beam Forming and Steering

The total radiation pattern of an antenna array is obtained via a linear superposition of all embedded element patterns (EEPs)—the radiation pattern of an element excited in the array with all other elements terminated—weighted by the respective excitation amplitude and phase of the antenna elements. However, the mutual coupling that one element experiences in the full array environment is largely dependent on its location in the array and the utilized separation distance between the elements, and as a consequence the internal EEPs may differ substantially from element to element.

Instead, the array factor is an intuitive way of illustrating the array concept in terms of beam forming and beam steering [28, 34]. By omitting the impact of mutual coupling on the radiation performance of each respective antenna, the total gain pattern, $G_{\mathrm{tot}}(\theta, \phi)$, of an array consisting of identical antenna elements may be approximated as

$$G_{\mathrm{tot}}(\theta, \phi) = |A(\theta, \phi)|^2 G_{\mathrm{elem}}(\theta, \phi)\,, \tag{2.5}$$

where $G_{\text{elem}}(\theta, \phi)$ is the element gain and $A(\theta, \phi)$ is the array factor. In turn, the array factor depends on the location of the antennas in the array configuration, and the complex excitation coefficient of each antenna as

$$A(\theta, \phi) = \sum_{n=1}^{N} a_n \mathrm{e}^{\mathrm{j}\varphi_n} \mathrm{e}^{\mathrm{j}\boldsymbol{k}\cdot\boldsymbol{r}_n}\,, \tag{2.6}$$

where $\boldsymbol{k} = k(\sin\theta\cos\phi\,\hat{\boldsymbol{x}} + \sin\theta\sin\phi\,\hat{\boldsymbol{y}} + \cos\theta\,\hat{\boldsymbol{z}})$ with $k = 2\pi/\lambda$ being the wavenumber, and a_n and φ_n are the excitation amplitude and phase, respectively, of the n:th antenna located at position $\boldsymbol{r}_n$.

The effect that the array configuration has on the achieved gain is illustrated here for an $N_y \times 1$ linear array of isotropic radiators along the $\hat{\boldsymbol{y}}$-axis with a uniform separation distance d_y. The configuration is shown in Figure 5. If the antennas are excited with equal magnitude and with a linear phase shift φ, *i.e.*, $\varphi_n = n\varphi$, the array factor becomes:

$$A(\theta, \phi) = \frac{1}{N_y} \sum_{n=0}^{N_y-1} \mathrm{e}^{\mathrm{j}n\psi}\,, \tag{2.7}$$

where

$$\psi = kd_y \sin\theta \sin\phi + \varphi\,. \tag{2.8}$$

The introduced progressive phase shift ψ denotes the phase shift between the elements when incorporating the observation angles θ and ϕ. The expression in (2.7) can be written in the form [34]

$$A(\theta, \phi) = \frac{\sin(N_y\psi/2)}{N_y \sin(\psi/2)} \mathrm{e}^{\mathrm{j}(N_y-1)\psi/2}\,, \tag{2.9}$$

such that the gain of the array is

$$|A(\theta, \phi)|^2 = \left| \frac{\sin(N_y\psi/2)}{N_y \sin(\psi/2)} \right|^2 . \tag{2.10}$$

It is evident from (2.10) that the array factor results in beam forming, and that it attains its maximum when the progressive phase shift ψ is zero or multiples of 2π, which translates into corresponding angular directions (θ, ϕ). Note that the above expressions can easily be expanded to treat planar or three-dimensional (3D) arrays, which would result in the total array factor being the product of the array factors along the considered dimensions.

The radiation pattern of the array factor in the xy-halfplane ($x \geq 0$) is illustrated in Figure 6 for varying N_y and d_y. The elements are excited in phase with $\varphi = 0°$, which corresponds to the beam being launched in the direction orthogonal to the array alignment, *i.e.*, the broadside direction. As seen, the maximum gain increases with both increasing N_y and increasing d_y. This can be put in relation to (2.4), stating that for a fixed frequency the gain is related to the antenna aperture which increases both with N_y and d_y.

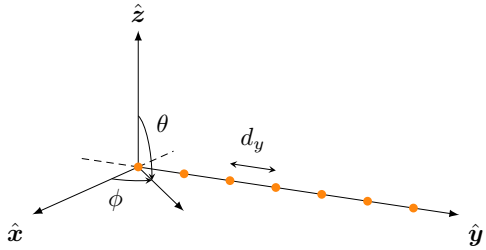

Figure 5: The considered array configuration; a linear $N_y \times 1$ array along the $\hat{\boldsymbol{y}}$-axis with a uniform separation distance d_y. The polar angle θ and azimuthal angle ϕ are also depicted.

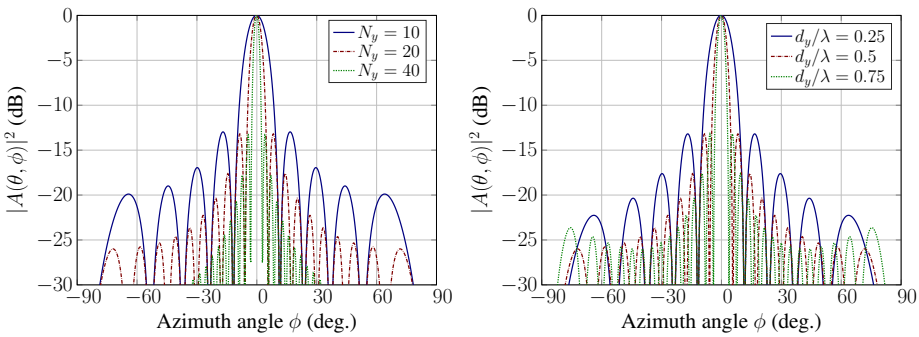

(a) (b)

Figure 6: Normalized azimuthal radiation pattern of the isotropic $N_y \times 1$ array for: (a) varying N_y with $d_y = \lambda/2$, and (b) varying d_y with $N_y = 20$.

By controlling the excitation phase of the elements, the direction of maximum radiation can be steered [28,34]. Since (2.10) attains its maximum when $\psi = 2\pi l$, $l = 0, \pm 1, \pm 2, \ldots$, the beam can be steered towards the (θ_0, ϕ_0)-direction by employing the phase shift

$$\varphi = -kd_y \sin\theta_0 \sin\phi_0 \,. \tag{2.11}$$

If it is desirable to only steer the beam in the xy-plane, then $\theta_0 = 90°$ and (2.11) boils down to $\varphi = -kd_y \sin\phi_0$. The beam steering principle is illustrated in Figure 7 for three maximum directions ϕ_0. As seen, a more oblique steering angle results in a broader beam, *i.e.*, a smaller maximum gain. Again referring to (2.4), this effect can be put in relation to that the antenna aperture is perceived as smaller along the direction of the main lobe as the beam is steered off-broadside.

For endfire mode operation, which corresponds to launching the beam along the axis of the array [28,35], the azimuth steering angle $\phi_0 = 90°$ and the phase shift in (2.11) becomes

$$\varphi = -kd_y \,. \tag{2.12}$$

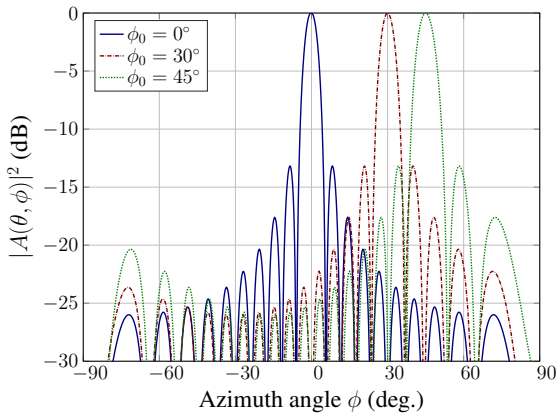

Figure 7: Normalized azimuthal radiation pattern of an isotropic 20×1 array with $d_y = \lambda/2$ for various steering angles ϕ_0.

A classical paper by Hansen-Woodyard [36] derived a slightly modified version of this phase shift to maximize the directivity of arrays consisting of a large number of elements:

$$\varphi = -(kd_y + 2.94/N_y)\,. \tag{2.13}$$

A comparison of employing the two phase shifts for endfire mode operation of a 40×1 array is shown in Figure 8. An increase in the directivity can be observed; however, employing any of these two phase shifts causes the array to be poorly matched due to the strong mutual coupling between the elements that arises as a consequence of the energy being launched along the axis of the array. In Paper I, a comparison study is presented that focuses on how this coupling impacts the numerical accuracy of the macro basis function method (a numerical technique presented in Section 4.4). In Paper II, an optimization routine is presented for synthesizing endfire excitation coefficients such that the overall matching of the array is not compromised.

Just as demands are put on an array's beam forming and steering characteristics, side lobe level constraints are also frequently enforced to ensure that power transmitted or received in undesirable directions is suppressed [28,37]. As a natural response to the development of the array technology, various synthesis techniques have been proposed with the purpose of tailoring the excitation of the antenna elements to meet the performance demands. For instance, the Dolph-Chebyshev weighting technique presented in 1946 is widely considered as one of the classical techniques for side lobe level control [37]. Since then, various optimization approaches have been presented in the literature—see for instance [38,39]—and over the course of the last 20 years much research has been devoted to synthesis techniques based on convex optimization [40–44]. This is also the focus of Paper II as mentioned above.

Grating lobes—main lobes that do not belong to the principal maximum

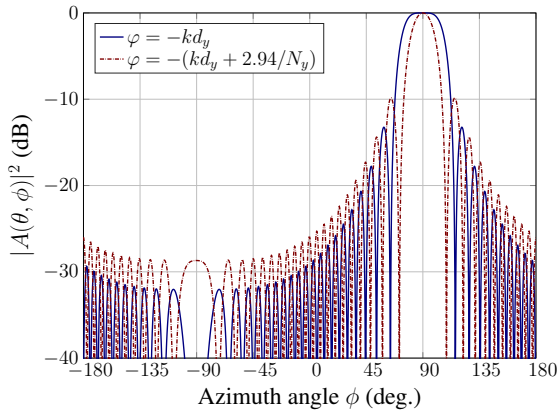

Figure 8: Normalized azimuthal radiation pattern of an isotropic 40×1 array with $d_y = \lambda/4$ for two different endfire excitations; ordinary (blue) and Hansen-Woodyard (H-W) (dashed red).

($l = 0$)—can be viewed as spectral images arising as a result of the utilized separation distance, since the array is not continuous but rather sampled at each point where an antenna is located. They are in most antenna applications undesirable, and need to be treated separately from side lobes. For a given steering direction towards ϕ_0 with $\theta_0 = 90°$, the range of ψ can be found by inserting (2.11) into (2.8) and using that $-1 \leq \sin\phi \leq 1$:

$$-kd_y(1 + \sin\phi_0) \leq \psi \leq kd_y(1 - \sin\phi_0)\,. \tag{2.14}$$

This range can thus be used to track whether grating lobes will be present, and if so, at which angles they will occur (using $\psi = \pm 2\pi l$ with $l \geq 1$). The range in (2.14) depends on both d_y and ϕ_0, and to completely avoid grating lobes the separation distance should be selected as $d_y \leq \lambda/2$ resulting in $kd_y \leq \pi$. Evidently, there exists a compromise between an array's directivity and beam steering capability; a longer separation distance increases the directivity as the array is made larger, but simultaneously decreases the maximum steering angle for which no grating lobes can occur. Synthesis techniques for grating lobe suppression therefore often involve a mutual treatment of the overall grid of the antenna configuration—*e.g.*, by avoiding a uniform rectangular grid—and the antenna excitations themselves [44–46].

2.3 Network Analysis of Multi-Port Arrays

In addition to the far field characteristics discussed in the previous section, it is also of interest to quantify the mutual coupling and impedance matching of an antenna array. These quantities are retrieved from the defined voltages and currents in the antenna ports, and as such, they can be acquired by representing

the array—consisting of N antennas—as a multi-port system, *i.e.*, as an N-port microwave network [47]. This circuit model representation requires that the scattering parameters of the array are known, and offers versatility in the selection of the underlying feeding network since such a network can be modeled using conventional transmission line or circuit theory subsequent to acquiring the scattering parameters of the array by full wave simulations or measurements [47].

The scattering matrix $\mathbf{S}$ is defined in relation to the ingoing and outgoing voltage waves at the antenna ports as:

$$\boldsymbol{b} = \mathbf{S}\boldsymbol{a}\,. \tag{2.15}$$

Here,

$$\mathbf{S} = \begin{bmatrix} S_{1,1} & S_{1,2} & \dots & S_{1,N} \\ S_{2,1} & S_{2,2} & \dots & S_{2,N} \\ \vdots & \vdots & \ddots & \vdots \\ S_{N,1} & S_{N,2} & \dots & S_{N,N} \end{bmatrix}, \tag{2.16}$$

and the vectors $\boldsymbol{b} = [b_1, b_2, \dots, b_N]^{\mathrm{T}}$ and $\boldsymbol{a} = [a_1, a_2, \dots, a_N]^{\mathrm{T}}$ represent the outgoing and ingoing voltage waves in all N ports, respectively. Reciprocity yields that $\mathbf{S}$ is symmetric, *i.e.*, $\mathbf{S} = \mathbf{S}^{\mathrm{T}}$, and it is also assumed to be invertible. The element $S_{n,m}$ is found by driving port m with an incident wave of voltage a_m and reading the reflected wave b_n coming out of port n. This implies that the incident waves on all other ports should be set to zero, and thus that the ports are terminated with a matched load to avoid reflections [47]. Consequently, the scattering matrix is retrieved for specified characteristic impedances—determined by the matched loads—of the transmission lines connected to all N antenna ports.

The scattering matrix can however be transformed in post process to treat arbitrary characteristic impedances. The voltage waves in the port of antenna n are related to the corresponding voltage V_n and current I_n at that particular reference plane as [48]:

$$\begin{aligned} V_n &= a_n + b_n\,, \\ \text{and} \quad I_n &= (a_n - b_n)/Z_{\mathrm{c},n}\,. \end{aligned} \tag{2.17}$$

The characteristic impedance of the n:th port is denoted $Z_{\mathrm{c},n}$. A circuit model of an N-port array is depicted in Figure 9, where all these quantities are depicted. The following matrix form is then obtained by introducing the diagonal matrix $\mathbf{Z}_{\mathrm{c}}$ representing the characteristic impedance in all N ports:

$$\begin{aligned} \boldsymbol{V} &= \boldsymbol{a} + \boldsymbol{b}\,, \\ \text{and} \quad \boldsymbol{I} &= \mathbf{Z}_{\mathrm{c}}^{-1}(\boldsymbol{a} - \boldsymbol{b})\,. \end{aligned} \tag{2.18}$$

The admittance matrix $\mathbf{Y}$, defined by $\boldsymbol{I} = \mathbf{Y}\boldsymbol{V}$, relates the currents to the voltages, and insertion of (2.18) into this definition yields the following expression for $\mathbf{S}$ in terms of $\mathbf{Y}$ and $\mathbf{Z}_{\mathrm{c}}$:

$$\mathbf{S} = (\mathbf{I} + \mathbf{Z}_{\mathrm{c}}\mathbf{Y})^{-1}(\mathbf{I} - \mathbf{Z}_{\mathrm{c}}\mathbf{Y})\,. \tag{2.19}$$

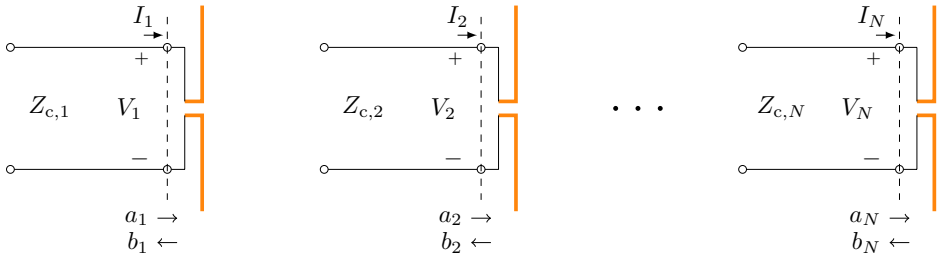

Figure 9: Circuit model equivalent of an array configuration. The antenna ports are marked by the dashed lines and constitute the reference planes for the ingoing (and outgoing) voltage waves a_n (and b_n), with $n = 1, 2, \ldots, N$. An arbitrary feeding network may be connected to the left hand ports of the antennas.

The identity matrix is $\mathbf{I}$; not to be confused with the current vector $\boldsymbol{I}$. Solving (2.19) for $\mathbf{Y}$ using the reference characteristic impedance matrix $\mathbf{Z}_0 = Z_0\mathbf{I}$ and the corresponding scattering matrix $\mathbf{S}_0$ gives:

$$\mathbf{Y} = \frac{1}{Z_0}(\mathbf{I} - \mathbf{S}_0)(\mathbf{I} + \mathbf{S}_0)^{-1}\,. \tag{2.20}$$

Inserting (2.20) into (2.19) results in, after extensive matrix manipulation, the following relation between the transformed matrix $\mathbf{S}$ and the reference matrix $\mathbf{S}_0$:

$$\begin{aligned} \mathbf{S} &= (\mathbf{I} + \boldsymbol{\Gamma}\mathbf{S}_0)^{-1}(\boldsymbol{\Gamma} + \mathbf{I}\mathbf{S}_0)\,, \\ \text{where}\quad \boldsymbol{\Gamma} &= \big(\mathbf{I} + \mathbf{Z}_\mathrm{c}/Z_0\big)^{-1}\big(\mathbf{I} - \mathbf{Z}_\mathrm{c}/Z_0\big)\,. \end{aligned} \tag{2.21}$$

In the case of equal transmission lines in all N antennas $\mathbf{Z}_\mathrm{c} = Z_\mathrm{c}\mathbf{I}$ and (2.21) simplifies to the expression presented in Paper II. It is thus feasible to investigate the matching of the system for various characteristic impedances. The matching of a single port in the full multi-port environment is quantified by the active reflection coefficient (ARC) [33, 49]:

$$\Gamma_n^\mathrm{a} = \frac{b_n}{a_n}\,. \tag{2.22}$$

Similarly, the total active reflection coefficient (TARC) is defined as the overall matching of all N ports [49]:

$$\Gamma_\mathrm{tot}^\mathrm{a} = \sqrt{\frac{\sum_{n=1}^{N}|b_n|^2}{\sum_{n=1}^{N}|a_n|^2}}\,. \tag{2.23}$$

These two single frequency metrics are thus very convenient for investigating the matching impact that a particular array excitation has on both a single port (the ARC) and the full multi-port system that the array constitutes (the TARC).

2.4 MIMO Antenna Systems

In today's communication networks multiple input multiple output (MIMO) antenna systems are also widely employed to increase channel capacity and improve reliability of communication links. The massive MIMO technology for instance—that intends to scale up conventional MIMO by exploiting arrays of several hundreds of elements in the base station and provide service for several tens of mobile terminals simultaneously—has emerged as a potential candidate for 5G wireless communication networks operating both in the conventional frequency bands (5 GHz or less), and at the mm-wave frequency bands [7, 14, 29, 30, 50].

A MIMO system uses multiple antennas in both transmit (Tx) and receive (Rx) to exploit multipath propagation and enable the usage of diversity schemes to increase the signal-to-noise ratio (SNR). Some key properties and technologies are mentioned here in brief, whereas a more comprehensive theoretical review on MIMO antenna systems can be found, *e.g.*, in [51, 52]. A MIMO channel with N Tx antennas and M Rx antennas can be modeled as

$$\boldsymbol{y} = \mathbf{H}\boldsymbol{x} + \boldsymbol{n}\,, \tag{2.24}$$

where $\mathbf{H} \in \mathbb{C}^{M\times N}$ is the channel matrix, $\boldsymbol{x} \in \mathbb{C}^{N\times 1}$ and $\boldsymbol{y} \in \mathbb{C}^{M\times 1}$ are the Tx and Rx signal vectors, respectively, and $\boldsymbol{n} \in \mathbb{C}^{N\times 1}$ is a noise vector. There are several ways to enhance capacity using MIMO antenna systems [19, 52], one of which is the support of multiple data streams in parallel known as spatial multiplexing. Additionally, diversity schemes can be used to transmit multiple copies of the same signal through independent channels to suppress the impact of fading (signal strength fluctuation). The diversity may be realized using, *e.g.*, spatial separation or different polarizations of the antennas, known as spatial and polarization diversity, respectively.

Naturally, a MIMO system's capability of increasing the capacity depends on several parameters, such as the propagation environment, spatial correlation and mutual coupling between the Tx or Rx antennas, and channel state information. For instance, if the channel is known to the multiple antenna transmitter, the proper weight coefficients can be applied to the antenna elements to realize the beam forming and steering principle resulting in increased transmit gain in the desired direction and thus increased SNR. Accordingly, and as discussed in Section 1, the implementation of antenna arrays in future mm-wave 5G UE devices is a widely proposed solution to overcome the higher losses occurring at mm-wave frequencies [9, 10, 15, 18].

2.5 Metrics for Millimeter Wave User Equipment

The utilization of phased arrays in the UE operating at mm-wave frequencies implies that it is essential to evaluate the beam steering characteristics of any proposed antenna design and array configuration. In a mobile terminal for instance, the chassis and phone case will have a distortion effect on the radiation pattern

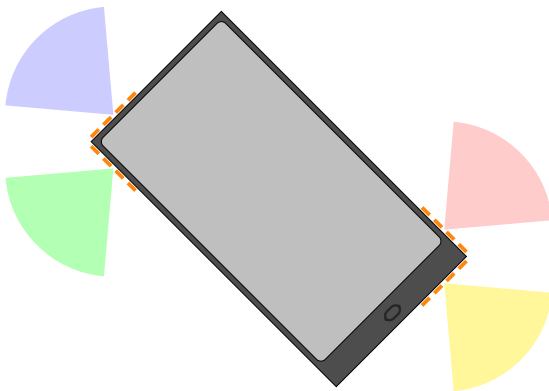

Figure 10: Enhancing the spatial coverage of mm-wave 5G cellular handsets using multiple phased arrays (shown in orange).

of the array, and furthermore inherently limit radiation to a sub-hemispherical coverage region [19]. Thus, multiple arrays need to be combined to achieve omnidirectional coverage, as illustrated in Figure 10. For this purpose, two metrics are introduced to evaluate the beam steering capability of phased array systems in the UE: 1) the total scan pattern merging the array patterns for all applicable phase shift configurations, and 2) the coverage efficiency:

$$\eta_{\mathrm{c}} = \frac{\text{Coverage Solid Angle}}{\text{Maximum Solid Angle}} = \frac{\Omega_{\mathrm{c}}}{\Omega_0}\,. \tag{2.25}$$

The total scan pattern gain, G_{TS}, is evaluated with respect to a threshold gain, G_{min}, over Ω_0 to obtain Ω_{c}:

$$\Omega_{\mathrm{c}} = \int_{\Omega_0} h(G_{\mathrm{TS}}(\Omega))\,\mathrm{d}\Omega\,, \tag{2.26}$$

where the step function h is defined as:

$$h(G_{\mathrm{TS}}) = \begin{cases} 1\,, & \text{if } G_{\mathrm{TS}} \geq G_{\mathrm{min}} \\ 0\,, & \text{if } G_{\mathrm{TS}} < G_{\mathrm{min}}\,. \end{cases} \tag{2.27}$$

This fairly general performance metric can be further specified to treat, *e.g.*, different polarizations, user impact and the beam steering efficiency of sub array configurations [8,17]. In Paper III, these metrics are used in a preliminary study on mm-wave array configurations of two microstrip antenna designs integrated on a UE platform.

Another critical point of consideration is that of human exposure to RF energy; wireless electronic devices that emit RF EMFs need to comply with regulatory requirements to ensure that the user is not exposed to harmful doses [53,54]. Below certain transition frequencies, ranging between 3 GHz and 10 GHz depending on the specific regulation guidelines [53–55], restrictions on EMF exposure

are specified in terms of the specific absorption rate (SAR); a metric quantifying the power absorbed per mass of tissue (W/kg). For frequencies above the transition limit, where a multitude of the frequency band candidates for the 5G wireless communication networks lies [6, 14, 56], this metric changes to the free space power density ($\mathrm{W/m^2}$) instead [53,57,58]. The main reason for this is that the penetration depth decreases substantially with increasing frequency, making absorbed energy difficult to measure accurately [16]. The time-averaged power density, $\boldsymbol{S}$, is defined as [28]:

$$\boldsymbol{S}(\boldsymbol{r},\omega) = \frac{1}{2}\,\mathrm{Re}\left\{\boldsymbol{E}(\boldsymbol{r},\omega)\times\boldsymbol{H}^{*}(\boldsymbol{r},\omega)\right\}, \tag{2.28}$$

where $\omega = 2\pi f$ is the angular frequency, $\boldsymbol{E}$ is the electric field, and $\boldsymbol{H}^{*}$ is the complex conjugated magnetic field.

The power density is retrieved over a planar surface at a predetermined distance away from the AUT, and compliance is studied in terms of both the spatial peak and the spatially averaged power density. As the UE is situated in the immediate vicinity of the human body in almost all user modes, this has traditionally implied that the user resides in the reactive near field region of the antenna, making it problematic to quantify the true power density. The distance d at which the reactive near field transcends into the radiative near field—although not strictly defined as it varies depending on the antenna size and type—can be roughly approximated to lie in the range [28, 59]:

$$\lambda/(2\pi) \leq d \leq 0.62\sqrt{D^3/\lambda}\,, \tag{2.29}$$

where the lower limit refers to electrically small antennas, and the upper limit holds for antennas whose largest dimension $D \gg \lambda$. Accordingly, for arrays that operate at frequencies above 10 GHz ($\lambda \leq 3\,\mathrm{cm}$), and whose dimensions span a couple of wavelengths, the radiative near field region occurs very close to the antenna (arguably within a mm–cm range), enabling the power density to be estimated at close ranges.

Nevertheless, measuring the power density when considering wavelengths on a mm-wave scale constitutes a challenge since a margin of error of 1 mm corresponds to, *e.g.*, one fifth of a wavelength at 60 GHz. Thus, absolute positioning and alignment of the antenna under test (AUT) with respect to the planar evaluation surface need to be accurately determined to avoid large errors in the retrieved amplitude and phase. In turn, this puts stringent requirements on the measurement techniques applicable to study EMF exposure compliance at mm-wave frequencies. This issue is addressed in Paper IV, where a measurement and data post processing technique based on the inverse source method (discussed further in Section 3) is presented together with a novel probe correction procedure.

3 Millimeter Wave Imaging Systems

In the most general sense, millimeter wave (mm-wave) imaging is the science of utilizing electromagnetic (EM) fields in the 30 GHz to 300 GHz region—where the corresponding wavelength ranges between 10 mm and 1 mm—to provide an image of a structure, a material or a field region around, *e.g.*, a transmitting antenna operating in the said frequency range [20, 21]. To study EMF exposure compliance at mm-wave frequencies for instance, the aim is to reconstruct the near field on a finite surface at a predetermined distance from the AUT [16,57]. The other application of interest here—the reader is referred to the overviews provided in [20,21] for more details on the extensive practical usages of mm-wave imaging—is EM NDT of composite structures; structures that are composed of low permittivity and low loss materials and are utilized extensively in radomes and aircraft structural components [60]. As such, EM NDT is used in the aerospace industry as a step in the production chain of composite structures to evaluate each manufactured component and detect potential geometric or electromagnetic anomalies. For instance, a 10 GHz imaging system based on source reconstruction was utilized in [22, 61, 62] as a radome diagnostics tool. Operating at the even higher mm-wave frequency bands offers some substantial benefits in term of a compact measurement setup (under the assumption that the device under test (DUT) is sufficiently small) and high resolution at the expense of a more shallow penetration depth, which is of less concern due to the characteristics of the composites.

3.1 Experimental Setup and Post Processing

The measurement approach adapted here is the planar scanning technique, where the field is sampled over a finite planar surface at some distance away from either the AUT—the Tx antenna—or, in the NDT scenario, the DUT that has been illuminated by the Tx antenna [59]. The field is sampled over a rectangular grid by moving an Rx probe, chosen as an open-ended rectangular waveguide, in a meander-like fashion over the measurement surface using a specified spatial increment. The probe movement is realized using electronically steerable THORLABS LTS300/M positioners providing an alignment accuracy on a μm-scale [63]. A Rohde & Schwarz ZVA 67 GHz vector network analyzer (VNA) is used to register the signals in the frequency domain across a user-defined bandwidth, by treating the complete setup as an electrical network and registering the scattering parameters in the respective ports of the system at each discrete frequency point [47]. The input and output parameters to the positioners and the VNA are remotely controlled using a laptop computer and in-house written Matlab scripts. Finally, absorbers are placed around the setup to suppress multipath propagation caused by reflection and diffraction from the surrounding environment. The complete setup is mounted on a Newport RS 2000 optical table to minimize deflection and realize an accurate alignment that is stable over time. Accordingly, the optical table permits the experimental setup to easily be recreated at a later instance if

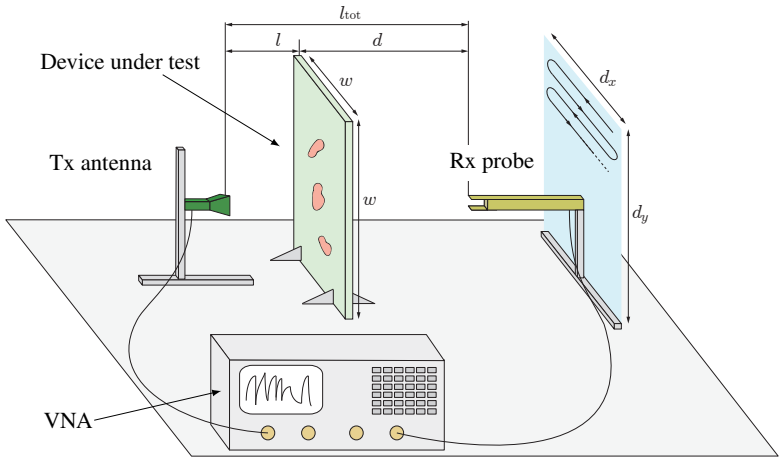

Figure 11: Schematic of the experimental setup used for transmission-based NDT measurements of a planar device under test (DUT).

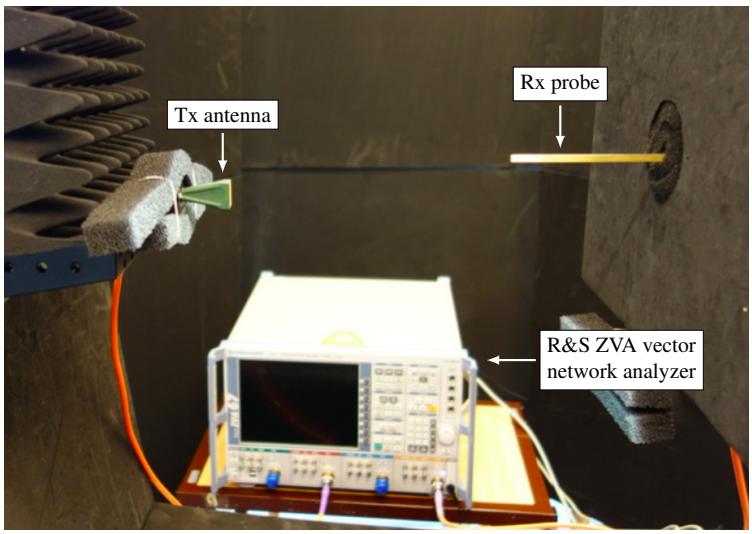

Figure 12: The experimental setup of the measurement system at 60 GHz used in Paper IV, with surrounding absorbers and a standard gain horn as the antenna under test (AUT).

necessary.

A schematic of the experimental setup used for the transmission-based NDT measurements in Paper V is depicted in Figure 11. Photographs of the setups used in Papers IV and VI are shown in Figures 12 and 13, respectively.

Despite surrounding the complete setup with absorbers, it is unpreventable

that multipath propagation will have an impact on the received signal. Since multipath components experience different time delays, time domain gating can effectively be applied to mitigate this problem [64]. The procedure involves applying an inverse fast Fourier transform (FFT) to the measured data to view it in the time domain, and subsequently filtering out the spurious signals using an appropriate windowing function. The time domain resolution and range are inversely proportional to the frequency bandwidth and resolution, respectively, and thus must the frequency domain settings of the VNA be set accordingly to ensure that the gating can be applied.

To avoid strong EM absorption the scan is conducted in the radiative near field region of the AUT—that is, outside the reactive near field region—where the radiation fields dominate yet the field pattern in general still exhibit a radial dependence. The directivity of the AUT should also be considered as to assure that sufficient energy is captured by the finite measurement surface. Moreover, choosing the sample increment as $\Delta \leq \lambda/2$ ensures that no aliasing occurs in accordance with the Nyquist-Shannon theorem [65]. In some cases sampling can be made sparser to decrease the otherwise exceedingly long scan time. This comes at the expense of aliasing; depending on the geometrical properties of the experimental setup however, the aliasing might have little or no effect on the final image.

As the open-ended waveguide is a non-ideal probe and its spatial relation to the rest of the experimental setup is dynamic, it has a non-local interaction with its field environment that depends both on its own EM characteristics and its position on the measurement surface [59,66,67]. In essence, this implies that—at each sampling point—what the VNA actually registers on the receiving end is a complex-valued voltage signal accounting for the full probe interaction. A probe correction technique is thus required to obtain the actual field in the sampling points. Standard probe correction techniques conventionally exploit *a priori* information on the probe's EM characteristic to atone for this effect. Paper IV presents a novel probe correction technique that does not require any information on the utilized probe, but instead uses data from a second measurement of an electrically small aperture to remove the probe impact. The interested reader is referred to [59] for an elaborate overview of the history of planar, cylindrical and spherical near field scanning methods and the accompanying probe correction techniques.

3.2 Image Retrieval Algorithms

Once the field has been acquired across the measurement surface, the objective is to retrieve an image of, *e.g.*, the material parameters, the electric and/or magnetic currents, or the EM fields, on a surface situated closer to the Tx antenna (in the NDT scenario the surface is chosen as a cross section of the planar DUT) than the actual measurement surface. This type of problem is referred to as either an inverse source or inverse scattering problem [68–70]. The former aims at finding

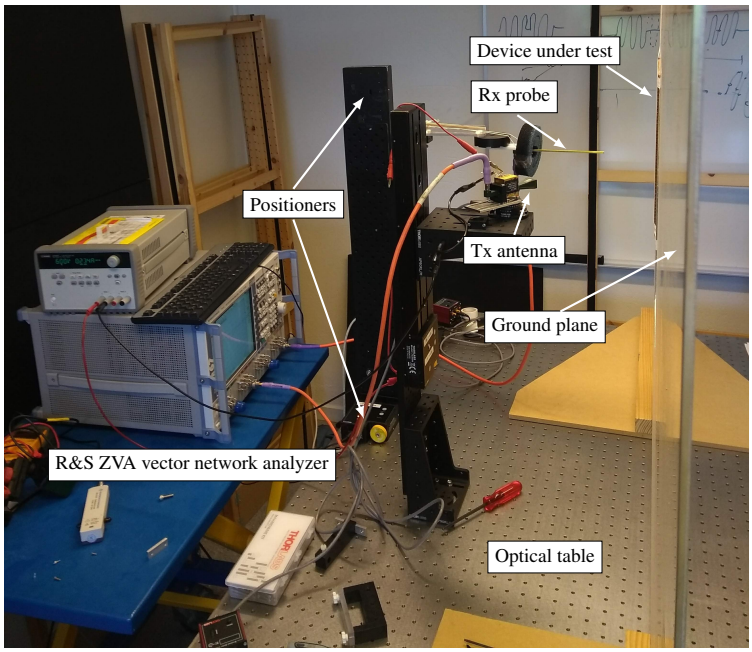

Figure 13: The experimental setup of the measurement system at 60 GHz used in Paper VI. The device under test (DUT) is mounted on top of a metallic ground plane, and the spatially fixed Tx antenna illuminates the DUT from an oblique angle. The positioners that scan the Rx probe across the rectangular measurement surface are seen to the left.

the equivalent source currents, $\boldsymbol{J}$, given a radiated field, $\boldsymbol{E}$, whereas the latter amounts to finding the characteristics of the target in terms of, *e.g.*, geometrical shape or regions of varying permittivity $\varepsilon(\boldsymbol{r})$ (dielectric contrast). The properties of the operator describing the relationship between the given and sought-after quantities is controlled by the physics of the problem, which can be formulated using field integral equations (see Section 4). However, while the inverse source problem can be described using linear operators, the inverse scattering problem is non-linear due to the fact that the permittivity or the dielectric contrast constitutes the unknown [68]. Accordingly, suitable reformulations or approximations are commonly adopted to formulate the problem in a linear sense [71–73].

The image retrieval algorithms considered here are based on the matrix form of the electric field integral equation (EFIE)—discussed in greater detail in Section 4—which reads:

$$\boldsymbol{E} = \mathbf{N}\boldsymbol{J}\,. \tag{3.1}$$

Here, the column vector $\boldsymbol{E} \in \mathbb{C}^{N\times 1}$ contains the known electric field in the N sampling points, the column vector $\boldsymbol{J} \in \mathbb{C}^{M\times 1}$ contains the M unknowns representing the discretized electric current on the reconstruction surface, and $\mathbf{N} \in \mathbb{C}^{N\times M}$ is

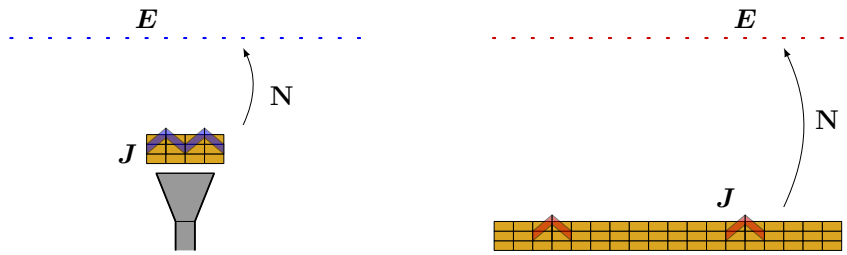

Figure 14: Numerical models of (3.1) used in the image retrieval algorithms under different scenarios. Left: A small planar surface is used to model an antenna aperture in terms of equivalent electric currents. Right: A larger surface is used to model, *e.g.*, a planar device under test (DUT), resulting in exceedingly large dimensions of the operator **N**.

the moment matrix operator describing the linear relationship between the two. Numerical models are depicted in Figure 14, where the reconstruction surfaces are discretized into rectangular mesh cells with rooftop functions acting as local basis functions. If the matrix **N** is non-invertible and ill-conditioned, the problem may be regularized and solved by constructing the pseudo-inverse using the truncated singular value decomposition (SVD) method [70], as disclosed in Papers IV, V and VI. With the equivalent source currents obtained, the fields in any region of interest may be found through (3.1) using the appropriate operator **N**.

The NDT scenario is also perfectly suited for additional regularization techniques to be applied. Under the reasonable assumption that the DUT only contains anomalies that are small in size or induce weak scattering, the problem may be formulated in a compressive sensing (CS) sense since the solution vector is known beforehand to only contain a few non-zero entries with respect to a predefined basis [74]. The CS technique utilizes L_1-regularization to search for a sparse solution under this precondition, and is particularly efficient in finding solutions to underdetermined linear problems [75]. The solution can further be recovered using far fewer samples than what is generally required by the Shannon-Nyquist sampling theorem, implying that it is feasible to substantially reduce the overall measurement time. These favorable properties of CS have prompted a rapid development of innovative solutions to a variety of EM problems concerning, *e.g.*, array synthesis [76], antenna diagnostics [77], and microwave imaging and inverse scattering [78, 79].

Employing an iterative optimization technique based on, *e.g.*, CS, requires the matrix-vector operations to be executed at every iteration. However, for exceedingly large values of N and M it becomes infeasible to even store the complete matrix **N**, and furthermore to perform any matrix-vector operations involving **N**. Under the condition that the measurement and reconstruction surfaces are parallel and are discretized identically, matrix-free operations can be performed in a time-efficient manner using classical FFT-algorithms [80, 81]; a

mere consequence of the then existing block Toeplitz properties of $\mathbf{N}$. A scenario where this is applicable is shown to the right in Figure 14.

4 Hybridized Method of Moments

The method of moments (MoM) is the main numerical technique for solving integral equations in EMs, and is further regarded as one of the predominant computational electromagnetics (CEM) methods around today [82–84]. In essence, CEM is the process of numerically addressing the interaction of EM fields with physical objects for the purpose of acquiring various EM quantities, *e.g.*, the radiation pattern of an antenna, or the RCS of a scatterer. CEM methods are based on computationally efficient approximations to Maxwell's equations, and commonly utilize a discretized version of either the physical object or the full 3D volume of interest to acquire a set of unknowns—referred to as the total degrees of freedom (DoFs)—that constitute the solution to the problem at hand. Many methods have been developed targeting specific problems of interest, and depending on the complexity and electrical size of the problem, it is important to utilize the proper method to acquire accurate results in a time efficient manner.

Integral equation methods such as the MoM were long regarded as ill-suited for electrically large problems, mainly because the matrix system associated with these solvers comprises a dense matrix requiring $\mathcal{O}(N^2)$ storage and a computational complexity scaling as $\mathcal{O}(N^3)$ [82, 83]. However, recent advancements in fast integral equation solvers and associated hybrid methods developed to increase time efficiency and reduce the memory requirements of standard MoM, has moved the technique to the forefront of CEM methods applicable to electrically large problems [82, 84].

4.1 The Dyadic Green's Function

The electromagnetic fields are assumed time-harmonic, *i.e.*, the time variation of the fields is sinusoidal and oscillates at an angular frequency ω. The time domain electric field $\boldsymbol{\mathcal{E}}(\boldsymbol{r}, t)$ can thus, using the time convention $\mathrm{e}^{\mathrm{j}\omega t}$, be written as

$$\boldsymbol{\mathcal{E}}(\boldsymbol{r}, t) = \mathrm{Re}\left\{\boldsymbol{E}(\boldsymbol{r}, \omega)\mathrm{e}^{\mathrm{j}\omega t}\right\}, \tag{4.1}$$

with $\boldsymbol{E}(\boldsymbol{r}, \omega)$ being the frequency domain electric field. Henceforth, the ω-term will be omitted for convenience.

The EFIE, that constitutes the foundation of the standard MoM solver for homogeneous medium and metallic scatterers, can be conveniently expressed in terms of the dyadic Green's function $\mathbf{G}(\boldsymbol{r}, \boldsymbol{r}')$ that represents the point source response to the Helmholtz vector wave equation [82]:

$$\nabla \times \nabla \times \boldsymbol{E}(\boldsymbol{r}) - k^2 \boldsymbol{E}(\boldsymbol{r}) = -\mathrm{j}\omega\mu \boldsymbol{J}(\boldsymbol{r}). \tag{4.2}$$

The wavenumber k is defined in terms of ω and the speed of light c as $k = \omega/c$, the permeability of the considered medium is μ, and $\boldsymbol{J}$ signifies a volume current density ($\mathrm{A/m^3}$). This equation can be derived with no approximations straight from Maxwell's equations [69], and is a common starting point for the modeling of wave propagation mechanisms and electromagnetic interactions. It can be shown that the fundamental solution to the equation,

$$\nabla \times \nabla \times \mathbf{G}(\boldsymbol{r}, \boldsymbol{r}') - k^2 \mathbf{G}(\boldsymbol{r}, \boldsymbol{r}') = -\mathbf{I}_3 \delta(\boldsymbol{r} - \boldsymbol{r}')\,, \tag{4.3}$$

where $\mathbf{I}_3$ is the identity dyadic and $\delta(\boldsymbol{r})$ is the Dirac delta function, is given by the dyadic Green's function $\mathbf{G}(\boldsymbol{r}, \boldsymbol{r}')$ in a homogeneous medium:

$$\mathbf{G}(\boldsymbol{r}, \boldsymbol{r}') = \left(\mathbf{I}_3 + \frac{\nabla\nabla}{k^2}\right) \frac{\mathrm{e}^{-\mathrm{j}k|\boldsymbol{r}-\boldsymbol{r}'|}}{4\pi \mid \boldsymbol{r} - \boldsymbol{r}' \mid}\,. \tag{4.4}$$

The dyadic Green's function operates as an exact propagator and represents the electric field in the observation point $\boldsymbol{r}$ that is generated by a point source situated in $\boldsymbol{r}'$. This key characteristic is the reason behind that the dyadic Green's function is such a convenient tool for expressing the integral equations numerically.

4.2 Matrix Formulation of the Electric Field Integral Equation

Consider the problem of a perfect electric conductor (PEC) structure—either representing an antenna or a scatterer— that resides in free space and is excited by means of either an active port (antenna) or an incident field (antenna or scatterer). The scenario is depicted in Figure 15. Since no magnetic currents may exist on the surface of the structure, *i.e.*, $\boldsymbol{M} = -\hat{\boldsymbol{n}} \times \boldsymbol{E} = 0$, any excitation will only induce a surface current density ($\mathrm{A/m^2}$), $\boldsymbol{J}$. Successively, the surface current density will radiate an electromagnetic field itself [69, 82], and it is this field that is of interest in the majority of all scattering and antenna problems. This field, depicted as the scattered field $\boldsymbol{E}_{\mathrm{sc}}$ in Figure 15, may only be retrieved once the unknown surface current density is obtained for the given excitation of the structure. The EFIE is a mathematical description of this phenomenon that utilizes the dyadic Green's function to relate the excitation of the structure, modeled by an incident electric field at the surface interface, to the induced surface current density:

$$\hat{\boldsymbol{n}} \times \boldsymbol{E}_{\mathrm{inc}}(\boldsymbol{r}) = \mathrm{j}k\eta_0 \hat{\boldsymbol{n}} \times \int_S \mathbf{G}(\boldsymbol{r}, \boldsymbol{r}') \cdot \boldsymbol{J}(\boldsymbol{r}')\, \mathrm{d}\boldsymbol{r}'\,. \tag{4.5}$$

Here, $\hat{\boldsymbol{n}}$ is the normal direction of the surface S, $\boldsymbol{E}_{\mathrm{inc}}(\boldsymbol{r})$ is the incident electric field assumed known, and η_0 is the intrinsic impedance in free space. In active antenna problems, $\boldsymbol{E}_{\mathrm{inc}}(\boldsymbol{r})$ is usually defined by the voltage produced by a port excitation over a specified discretized edge, divided by its length.

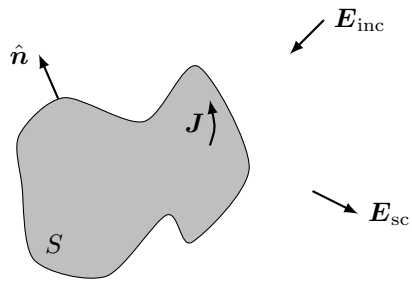

Figure 15: Scattering by a perfect electric conductor (PEC) structure with surface S.

The MoM—being a numerical computational tool for solving an integral equation—requires the EFIE to be discretized and expressed in matrix form, and to achieve this the surface current density is expanded using a set of N tangential, real-valued basis functions $\boldsymbol{\psi}_n(\boldsymbol{r})$, $n = 1, \ldots, N$:

$$\boldsymbol{J}(\boldsymbol{r}) = \sum_{n=1}^{N} I_n \boldsymbol{\psi}_n(\boldsymbol{r})\,. \tag{4.6}$$

Inserting this expansion into (4.5) gives:

$$\hat{\boldsymbol{n}} \times \boldsymbol{E}_{\text{inc}}(\boldsymbol{r}) = \mathrm{j}k\eta_0 \sum_{n=1}^{N} I_n \int_S \hat{\boldsymbol{n}} \times \mathbf{G}(\boldsymbol{r}, \boldsymbol{r}') \cdot \boldsymbol{\psi}(\boldsymbol{r}')\,\mathrm{d}\boldsymbol{r}'\,. \tag{4.7}$$

Since an $\boldsymbol{r}$ dependence is still present, a set of testing functions $\boldsymbol{w}_m(\boldsymbol{r})$, $m = 1, \ldots, N$ is introduced to test the equation and obtain the final matrix form. A common choice, known as Galerkin's method [85], is to use the basis functions as testing functions, *i.e.*, $\boldsymbol{w}_m(\boldsymbol{r}) = \boldsymbol{\psi}_m(\boldsymbol{r})$. Through dot multiplication with $\hat{\boldsymbol{n}} \times \boldsymbol{w}_m(\boldsymbol{r})$ and integration over the complete surface S, (4.7) can be written as a linear system of equations,

$$\int_S \boldsymbol{\psi}_m(\boldsymbol{r}) \cdot \boldsymbol{E}_{\text{inc}}(\boldsymbol{r})\mathrm{d}\boldsymbol{r} = \mathrm{j}k\eta_0 \sum_{n=1}^{N} I_n \int_S \int_S \boldsymbol{\psi}_m(\boldsymbol{r}) \cdot \mathbf{G}(\boldsymbol{r}, \boldsymbol{r}') \cdot \boldsymbol{\psi}_n(\boldsymbol{r}')\,\mathrm{d}\boldsymbol{r}'\mathrm{d}\boldsymbol{r}\,, \tag{4.8}$$

which, in turn, can be written in the matrix form

$$\boldsymbol{V} = \mathbf{Z}\boldsymbol{I} \tag{4.9}$$

by introducing the following elements:

$$\begin{aligned} V_m &= \int_S \boldsymbol{\psi}_m(\boldsymbol{r}) \cdot \boldsymbol{E}_{\text{inc}}(\boldsymbol{r})\,\mathrm{d}\boldsymbol{r}\,, \\ \text{and} \quad Z_{mn} &= \mathrm{j}k\eta_0 \int_S \int_S \boldsymbol{\psi}_m(\boldsymbol{r}) \cdot \mathbf{G}(\boldsymbol{r}, \boldsymbol{r}') \cdot \boldsymbol{\psi}_n(\boldsymbol{r}')\,\mathrm{d}\boldsymbol{r}'\,\mathrm{d}\boldsymbol{r}\,. \end{aligned} \tag{4.10}$$

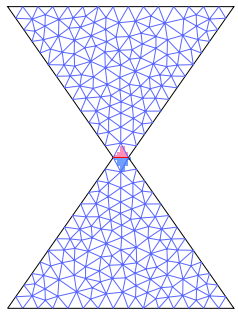

Figure 16: Triangular mesh of a bowtie antenna meant to operate at frequencies where its height is $\approx \lambda/2$.

Thus, the left-hand side in (4.9), $\boldsymbol{V} \in \mathbb{C}^{N\times 1}$, represents the excitation of the surface S and is commonly referred to as the excitation vector, whereas the matrix $\mathbf{Z} \in \mathbb{C}^{N\times N}$ represents the electromagnetic coupling between the basis functions and is referred to as the impedance matrix. The vector $\boldsymbol{I} \in \mathbb{C}^{N\times 1}$ contains the unknown current density coefficients I_n that are retrieved for a given excitation by solving (4.9).

For integral solvers, the geometrical objects of interest are commonly discretized into triangular mesh cells, and the standard choice of local basis functions is then the Rao-Wilton-Glisson (RWG) basis functions [86]; piece-wise linear basis functions spanning two triangle elements. A mesh view of a bowtie antenna, meant to operate at frequencies where the height of the antenna is $\approx \lambda/2$, is depicted in Figure 16. To ensure sufficient accuracy in the numerical solution, the mesh cell size should preferably not exceed $\lambda/10$ [82, 83]. Furthermore, if the geometry contains very detailed design features, the mesh needs to be refined in these regions to ensure sufficient resolution. As a result, it is not unusual to consider discretized models of trivial resonant type antenna elements where the number of DoFs, N, ranges somewhere between 100–1 000. For instance, the bowtie antenna seen in Figure 16 has been discretized such that $N \approx 800$. Furthermore, for more complex antenna geometries that incorporate an elevated level of detail as well as both metallic and dielectric materials, N may very well be in the order of 1 000–10 000.

Thus, in the context of arrays composed of a large number of antenna elements, recalling that storage and computational complexity scales as $\mathcal{O}(N^2)$ and $\mathcal{O}(N^3)$, respectively, it is deemed either extremely time-inefficient or simply impossible to obtain a numerical solution using conventional MoM on a standard desktop computer, assuming that no cluster or parallel computing is feasible. Rather, fast integral equation solvers and hybrid methods are needed to obtain accurate solutions and achieve accelerated computation [82].

4.3 The Adaptive Cross Approximation

The adaptive cross approximation (ACA) is an iterative algorithm that may be implemented as an add-on to the standard MoM in order to reduce memory usage and computational complexity [87]. In [87] it is claimed that computational complexity scales as $\mathcal{O}(N^{4/3}\log(N))$ for moderate size problems. The mathematical framework was first presented in [88] and the algorithm was later introduced in static and low-frequency EM and electromechanical problems in [89]. Since its introduction to EM, several papers have presented various improvement schemes [90, 91] and demonstrated the algorithm as one of several elements in fully hybridized MoM solvers [92].

Due to its completely algebraic nature, it can be applied to numerical source code independent of the underlying kernel function, and in [87] it was demonstrated that the ACA is particularly well-suited for the specific EM problem of accelerating the computation of coupling matrices between well-separated geometries. Consequently, its applicability to finite array problems is evident, since the full impedance matrix $\mathbf{Z}$ can be seen as a composition of the different sub-blocks representing the coupling between the antennas within the array. For an $N_x \times N_y$ uniform array of identical antennas the full impedance matrix, $\mathbf{Z} \in \mathbb{C}^{N_\mathrm{a}N\times N_\mathrm{a}N}$, can be written as

$$\mathbf{Z} = \begin{bmatrix} \mathbf{Z}_{1,1} & \mathbf{Z}_{1,2} & \dots & \mathbf{Z}_{1,N_\mathrm{a}} \\ \mathbf{Z}_{2,1} & \mathbf{Z}_{2,2} & \dots & \mathbf{Z}_{2,N_\mathrm{a}} \\ \vdots & \vdots & \ddots & \vdots \\ \mathbf{Z}_{N_\mathrm{a},1} & \mathbf{Z}_{N_\mathrm{a},2} & \dots & \mathbf{Z}_{N_\mathrm{a},N_\mathrm{a}} \end{bmatrix}, \tag{4.11}$$

where $N_\mathrm{a} = N_x N_y$ is the total number of antennas and each antenna comprises N DoFs. The ACA can be used to speed up the computation of the off-diagonal block matrices $\mathbf{Z}_{i,j} \in \mathbb{C}^{N\times N}$, $i \neq j$. In essence, it exploits the low rank nature of the matrix $\mathbf{Z}_{i,j}$—arising from that the coupling domains describe remote interaction—to approximate it using two lower rank matrices, $\mathbf{C}_{i,j} \in \mathbb{C}^{N\times r}$ and $\mathbf{R}_{i,j} \in \mathbb{C}^{r\times N}$:

$$\mathbf{Z}_{i,j} \approx \widetilde{\mathbf{Z}}_{i,j} = \mathbf{C}_{i,j}\mathbf{R}_{i,j}\,, \quad i \neq j\,. \tag{4.12}$$

The effective rank of $\mathbf{Z}_{i,j}$ is r; the number of columns and rows in the matrices $\mathbf{C}_{i,j}$ and $\mathbf{R}_{i,j}$, respectively. The decomposition of $\mathbf{Z}_{i,j}$ using (4.12) is depicted in Figure 17.

The iterative algorithm will continuously add elements to $\mathbf{C}_{i,j}$ and $\mathbf{R}_{i,j}$ until convergence is reached for a user-defined tolerance ϵ. The tolerance is commonly chosen somewhere between 10^{-2} and 10^{-4} for sufficient accuracy [87]. Hence, at iteration n, the ACA will terminate if

$$\|\mathbf{Z}_{i,j} - \widetilde{\mathbf{Z}}_{i,j}^{(n)}\|_\mathrm{F} \leq \epsilon\|\mathbf{Z}_{i,j}\|_\mathrm{F}\,, \tag{4.13}$$

where $\|\cdot\|_\mathrm{F}$ denotes the Frobenius norm [93]. Clearly, this requires both full knowledge of $\mathbf{Z}_{i,j}$ and that the matrix product $\mathbf{C}_{i,j}\mathbf{R}_{i,j}$ is computed. To avoid

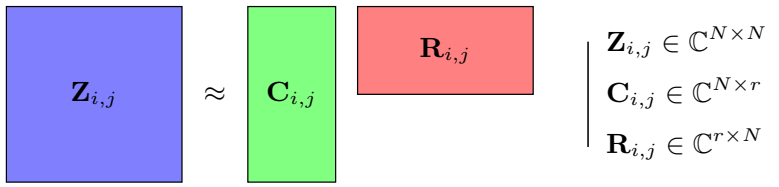

Figure 17: ACA decompositon of an impedance matrix $\mathbf{Z}_{i,j}$ into matrices $\mathbf{C}_{i,j}$ and $\mathbf{R}_{i,j}$.

this, the two norms can be approximated as

$$\begin{aligned} \|\mathbf{Z}_{i,j}\|_\mathrm{F} &\approx \|\mathbf{C}_{i,j}^{(n)}\mathbf{R}_{i,j}^{(n)}\|_\mathrm{F}\,, \\ \text{and} \quad \|\mathbf{Z}_{i,j} - \widetilde{\mathbf{Z}}_{i,j}^{(n)}\|_\mathrm{F} &\approx \|\boldsymbol{c}^{(n)}\|_2\,\|\boldsymbol{r}^{(n)}\|_2\,. \end{aligned} \tag{4.14}$$

Here, $\boldsymbol{c}^{(n)}$ and $\boldsymbol{r}^{(n)}$ are the column and row added at iteration n, respectively, and $\|\cdot\|_2$ denotes the L_2-norm. The first norm in (4.14) can be obtained without computation of the matrix product, as disclosed in the full algorithm description available in Appendix A.

The benefit of utilizing the ACA for computing the coupling between separated domains is demonstrated here for two $2\lambda \times 2\lambda$ PEC plates separated a distance d. The degrees of freedom N is 736 per plate such that the full coupling matrix is a 736×736 matrix. The effective rank r as a function of d is shown in Figure 18 for two different scenarios; a side-by-side alignment and an opposite alignment of the plates. As expected, it is seen how a more stringent tolerance results in a higher effective rank, and that r is decreasing as d increases. Moreover, for very closely spaced domains ($d < \lambda$), r essentially equals the full dimension of the coupling matrix, indicating that the efficiency of the ACA decreases as the domains are put closer together. This in turn implies that the algorithm is preferably employed only to block matrices representing the coupling between well-enough separated domains, *e.g.*, $d > \lambda/2$. Lastly, the opposite aligned plates experience a stronger coupling than those aligned side-by-side, resulting in a higher r.

4.4 The Macro Basis Function Method

The macro basis function (MBF) method is a means to reduce the DoFs in the linear equation system of standard MoM—defined by the number of local basis functions N—by constructing a set of M aggregated basis functions, the MBFs, thereby achieving a considerable compression if $M \ll N$ [92, 94]. There exist numerous variations of the method; for instance the characteristic basis function method [92,94], the synthetic function method [95], and the eigencurrent method [96]. Whereas the common concept of these is the same, the differences lie in how to generate the MBFs. The method has further been applied to antenna

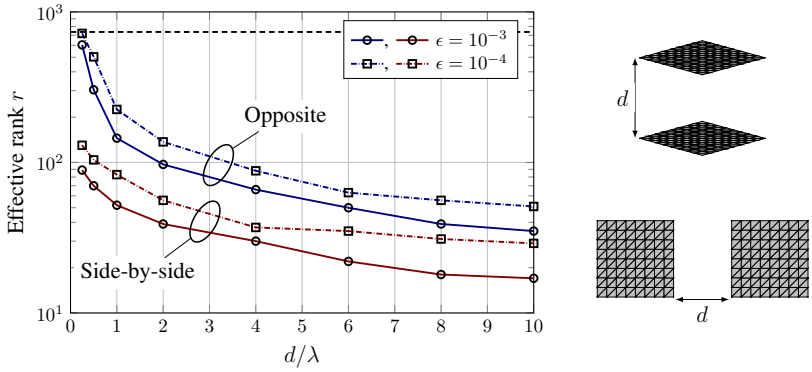

Figure 18: Effective rank r, as acquired from the ACA algorithm, of the coupling matrix $\mathbf{Z}$ between two $2\lambda \times 2\lambda$ PEC plates at various separation distances d for two choice of convergence threshold ϵ. The full dimension of $\mathbf{Z}$ is 736 which is displayed by the black dashed line.

and scattering problems as one of several acceleration methods; in [92] it was demonstrated combined with the ACA for large finite arrays with interconnected antennas, in [97] combined with the multilevel fast multipole method (MLFMM), and in [98] combined with the adaptive integral method (AIM).

The MBF method considered here is employed on the different sub-blocks constituting the full impedance matrix in (4.11) such that each one of these sub-blocks are compressed. For consistency, the analysis is again restricted to the problem of finite arrays consisting of identical antennas separated with uniform spacing in free space; however, the generality of the MBF method allows for employing it on other EM problems of more arbitrary geometries [92, 95, 97].

A sub-domain of the finite array is defined on which a set of induced currents will be used to characterize the MBFs. Intuitively, the sub-domain is chosen as a single antenna. The induced currents are generated through a set of N_e excitations, constituting the matrix $\mathbf{V}_\mathrm{e}$:

$$\mathbf{V}_\mathrm{e} = [\boldsymbol{V}_1, \boldsymbol{V}_2, \ldots, \boldsymbol{V}_{N_\mathrm{e}}]\,. \tag{4.15}$$

The excitations are chosen as any relevant port excitations of the sub-domain, and a set of plane waves for modeling the coupling from external sources. The number of angles of incidence N is chosen in a similar fashion as the spherical mode truncation to ensure proper excitation of the sub-domain [94, 99], *i.e.*, along the polar circle $N = ka + 10$ with a being the minimum radius of a sphere enclosing the sub-domain. The full plane wave spectrum is then obtained using a similar discretization in azimuth, and two orthogonal polarizations of the plane wave at each incident angle. The excitation scheme is illustrated in Figure 19. In addition, point dipoles can be positioned around the sub-domain to represent near field coupling [95].

The set of induced currents $\mathbf{I}_\mathrm{e}$ are now calculated using (4.9) given the self-

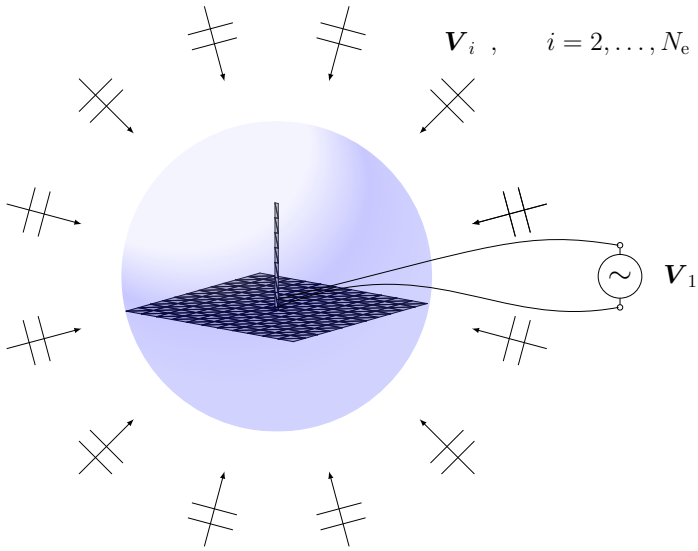

Figure 19: The set of N_e excitations for generating the induced currents constituting the foundation for the macro basis functions (MBFs). The example shows a monopole antenna above a ground plane with the enclosing sphere of minimum radius depicted in blue.

coupling impedance matrix, $\mathbf{Z}_\mathrm{sd}$, of the sub-domain:

$$\mathbf{I}_\mathrm{e} = \mathbf{Z}_\mathrm{sd}^{-1}\mathbf{V}_\mathrm{e}\,. \tag{4.16}$$

For reasonably small values of N, solving the above system comes at no considerable expense since $\mathbf{Z}_\mathrm{sd} \in \mathbb{C}^{N\times N}$ whereas the complete system of the finite array is represented by the matrix $\mathbf{Z} \in \mathbb{C}^{N_\mathrm{a}N\times N_\mathrm{a}N}$ in (4.11) where N_a is assumed large. However, if N is large (4.16) could constitute a computational bottleneck, implying that the method is best suited for problems where the sub-domain can be modeled using a not exceedingly large value of N.

Having obtained $\mathbf{I}_\mathrm{e}$, the MBFs are acquired by means of a singular value decomposition (SVD):

$$\mathbf{I}_\mathrm{e} = \mathbf{U}\boldsymbol{\Sigma}\mathbf{V}^\mathrm{H}\,. \tag{4.17}$$

Here, $\mathbf{U}$ and $\mathbf{V}$ are $N \times N$ and $N_\mathrm{e} \times N_\mathrm{e}$ unitary matrices containing the left- and right-singular orthonormal eigenvectors, respectively, and $\boldsymbol{\Sigma}$ is a rectangular diagonal matrix with the non-negative real-valued singular values σ_i, $i = \{1, 2, \ldots, \min\{N, N_\mathrm{e}\}\}$, ordered in descending magnitude, as its diagonal entries. The current distributions that may exist on the sub-domain—given the excitations used for generating the induced currents originally—can be expressed through the eigenvectors in $\mathbf{U}$, where the magnitude of the corresponding eigenvalue represents the independency (or importance) of that specific eigenvector in relation to the other eigenvectors [95]. As such, a compressed system of equa-

tions can be acquired by discarding the singular vectors of $\mathbf{U}$ whose normalized singular values are below a prescribed threshold τ,

$$\sigma_m/\sigma_1 \leq \tau\,, \quad m > M\,, \tag{4.18}$$

and defining the MBF compression matrix as

$$\widetilde{\mathbf{U}} = [\boldsymbol{u}_1,\, \boldsymbol{u}_2,\, \ldots,\, \boldsymbol{u}_M]\,, \tag{4.19}$$

where $\widetilde{\mathbf{U}} \in \mathbb{C}^{N\times M}$, $M \ll N$, and $\boldsymbol{u}_m$ represents the m:th eigenvector contained in $\mathbf{U}$. The MBF method aims to find an approximate solution vector $\widetilde{\boldsymbol{I}} \in \mathbb{C}^{N\times 1}$ to the original matrix equation in (4.9), *i.e.*, $\widetilde{\boldsymbol{I}} \approx \boldsymbol{I}$, that can be expressed as a linear combination of the eigenvectors in $\widetilde{\mathbf{U}}$:

$$\widetilde{\boldsymbol{I}} = \widetilde{\mathbf{U}}\boldsymbol{I}_{\text{mbf}}\,. \tag{4.20}$$

Evidently, the solution to the linear system of equations may then be represented by the M unknown current coefficients contained in $\boldsymbol{I}_{\text{mbf}} \in \mathbb{C}^{M\times 1}$. Accordingly, a compressed matrix formulation is obtained by left-hand multiplying both sides of (4.9) with $\widetilde{\mathbf{U}}^{\text{H}}$ and inserting (4.20) as the sought-after solution vector:

$$\boldsymbol{V}_{\text{mbf}} = \mathbf{Z}_{\text{mbf}}\boldsymbol{I}_{\text{mbf}}\,. \tag{4.21}$$

Here, the compressed impedance matrix and voltage vector are defined as:

$$\begin{aligned} \mathbf{Z}_{\text{mbf}} &= \widetilde{\mathbf{U}}^{\text{H}}\mathbf{Z}\widetilde{\mathbf{U}}\,, \quad \mathbf{Z}_{\text{mbf}} \in \mathbb{C}^{M\times M} \\ \boldsymbol{V}_{\text{mbf}} &= \widetilde{\mathbf{U}}^{\text{H}}\boldsymbol{V}\,, \quad \boldsymbol{V}_{\text{mbf}} \in \mathbb{C}^{M\times 1}\,. \end{aligned} \tag{4.22}$$

Once $\boldsymbol{I}_{\text{mbf}}$ is obtained as the solution to (4.21), the current density may be expressed through the local basis functions using (4.20).

The principle of the MBFs is illustrated in Figure 20, where the current distribution of three different eigenvectors contained in $\mathbf{U}$ is depicted together with the normalized magnitude of the corresponding singular values. For the large singular values ($> 10^{-2}$) the corresponding currents have a clear physical distribution, whereas the lower singular value ($\approx 10^{-8}$) results in a more spurious current distribution. Evidently, the overall compression is determined by the choice of the threshold value τ, which in turn determines the accuracy of the acquired MBF solution in relation to the full solution of the system. Typical values for τ ranges from 10^{-2} to 10^{-5} [92, 94, 95]. Table 1 shows three examples of achievable compression for different resonant type antennas using the MBF method implemented on top of the source code provided in [100].

For interconnected arrays, the procedure above requires slight modifications due to the interconnections between the antenna elements and the presence of several sub-domains. This problem is the main topic of Paper I, where two methods based on published research in [92] and [95] are compared.

Table 1: Compression examples for three different antennas as sub-domains, with $\tau = 10^{-3}$.

	N	M	M/N-ratio
Slot	1176	15	0.013
Monopole	367	10	0.027
Bowtie	4112	18	0.004

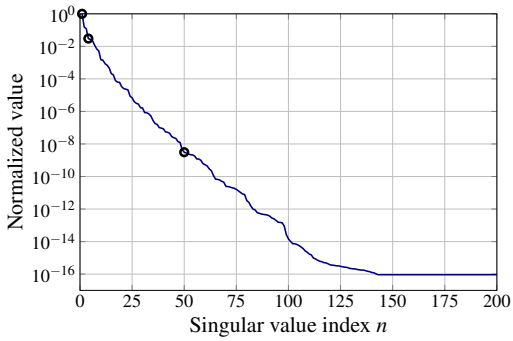

(a) The normalized singular values of $\mathbf{I}_e$, with σ_1, σ_4 and σ_{50} marked by black circles.

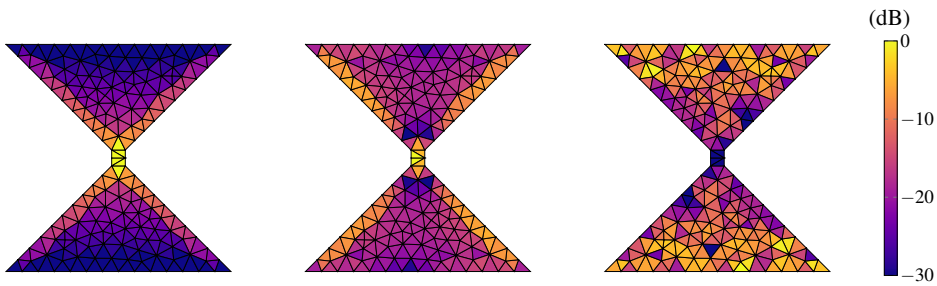

(b) Normalized current distribution of the three different eigenvectors $\boldsymbol{u}_1$, $\boldsymbol{u}_4$ and $\boldsymbol{u}_{50}$ of $\mathbf{I}_e$.

Figure 20: Example of utilizing eigenvectors, acquired from the singular value decomposition (SVD), as the macro basis functions (MBFs) to obtain a compressed system of equations. The sub-domain is a bowtie antenna similar to the one depicted in Figure 16.

4.5 Combining the ACA and the MBF method

The ACA and the MBF method were implemented as add-ons to a in-house standard MoM solver, see [27], to realize a hybridized solver capable of solving the problem of electrically very large arrays in a time efficient manner. All simulations in Paper II were run using this solver. Employing the ACA and the MBF method jointly yields the following compressed version of the full impedance

matrix found in (4.11):

$$\mathbf{Z}_{\mathrm{mbf}} = \begin{bmatrix} \widetilde{\mathbf{U}}^{\mathrm{H}}\mathbf{Z}_{1,1}\widetilde{\mathbf{U}} & \widetilde{\mathbf{U}}^{\mathrm{H}}\mathbf{C}_{1,2}\mathbf{R}_{1,2}\widetilde{\mathbf{U}} & \dots & \widetilde{\mathbf{U}}^{\mathrm{H}}\mathbf{C}_{1,N_{\mathrm{a}}}\mathbf{R}_{1,N_{\mathrm{a}}}\widetilde{\mathbf{U}} \\ \widetilde{\mathbf{U}}^{\mathrm{H}}\mathbf{C}_{2,1}\mathbf{R}_{2,1}\widetilde{\mathbf{U}} & \widetilde{\mathbf{U}}^{\mathrm{H}}\mathbf{Z}_{2,2}\widetilde{\mathbf{U}} & \dots & \widetilde{\mathbf{U}}^{\mathrm{H}}\mathbf{C}_{2,N_{\mathrm{a}}}\mathbf{R}_{2,N_{\mathrm{a}}}\widetilde{\mathbf{U}} \\ \vdots & \vdots & \ddots & \vdots \\ \widetilde{\mathbf{U}}^{\mathrm{H}}\mathbf{C}_{N_{\mathrm{a}},1}\mathbf{R}_{N_{\mathrm{a}},1}\widetilde{\mathbf{U}} & \widetilde{\mathbf{U}}^{\mathrm{H}}\mathbf{C}_{N_{\mathrm{a}},2}\mathbf{R}_{N_{\mathrm{a}},2}\widetilde{\mathbf{U}} & \dots & \widetilde{\mathbf{U}}^{\mathrm{H}}\mathbf{Z}_{N_{\mathrm{a}},N_{\mathrm{a}}}\widetilde{\mathbf{U}} \end{bmatrix}. \tag{4.23}$$

Since $\mathbf{Z}_{\mathrm{mbf}} \in \mathbb{C}^{N_{\mathrm{a}}M \times N_{\mathrm{a}}M}$ and $M \ll N$, the original problem may be solved time efficiently using this compressed system of equations.

Since the antennas in the array are identical the same MBF compression matrix is applied on all sub-blocks of $\mathbf{Z}$. If various sub-domains need to be considered, *e.g.*, if the array consist of several different antenna geometries or if electrical interconnections exist between the elements themselves, the procedure in Section 4.4 needs to be repeated for all singled-out sub-domains. As a consequence, the compression of an off-diagonal block matrix $\mathbf{Z}_{i,j}$ requires the usage of two MBF compression matrices:

$$\mathbf{Z}_{i,j}^{\mathrm{mbf}} = \widetilde{\mathbf{U}}_i^{\mathrm{H}}\mathbf{C}_{i,j}\mathbf{R}_{i,j}\widetilde{\mathbf{U}}_j\,. \tag{4.24}$$

Here, $\widetilde{\mathbf{U}}_i$ and $\widetilde{\mathbf{U}}_j$ are the compression matrices applicable to the corresponding sub-domains that antenna i and j belongs to, respectively.

In addition, further acceleration is feasible by exploiting the *a priori* information regarding existing symmetries in the finite array. The full impedance matrix $\mathbf{Z}$ found in (4.11) is transpose symmetric, *i.e.*, $\mathbf{Z}_{j,i} = \mathbf{Z}_{i,j}^{\mathrm{T}}$, implying that only the upper-triangular part in (4.23) needs to be computed. This would then require the Hermitian transpose in (4.22), (4.23) and (4.24) to be replaced by the ordinary transpose $\cdot^{\mathrm{T}}$ to maintain the symmetry. Moreover, a uniform configuration implies that a limited number of translation vectors are utilized to realize the full array geometry. These translational symmetries result in that both the full impedance matrix $\mathbf{Z}$ and its compressed version $\mathbf{Z}_{\mathrm{mbf}}$ are block Toeplitz matrices [101], which in turn can be exploited using a pre-process scheme to the MoM solver in order to minimize the number of sub-blocks that needs to be computed. For an arbitrary $N_x \times N_y$ uniform array it can be shown that it is only necessary to compute $N_xN_y + (N_x-1)(N_y-1)$ sub-blocks, *e.g.*, a 100×10 array only requires the computation of 1 891 sub-blocks which is less than 0.2 % of the actual existing 10^6 sub-blocks. The principle is illustrated in Figure 21 for a 4×2 uniform array using a colormap scheme to visualize the sub-blocks that are identical.

The computational speed-up that is realizable when utilizing the hybridized MoM discussed above is demonstrated in Table 1. The example configurations consist of bowtie antennas as the one in Figure 16, operating at the resonance frequency f_0. The antenna spacing is $\approx \lambda_0/2$. All acceleration schemes are implemented as add-ons to an existing standard MoM solver; implemented in

Table 2: Computation time required for various array configurations of bowties when the different acceleration schemes are employed.

	N	Standard MoM	ACA+MBF	+trans. sym.
8×3	15 432	242.0 s	7 s	2 s
40×4	102 880	N/A	3 min 1 s	6 s
100×10	643 000	N/A	96 min 38 s	1 min 38 s

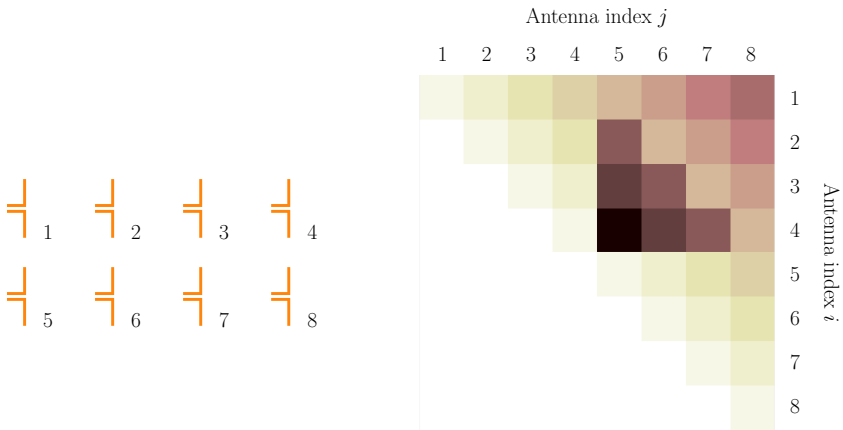

Figure 21: Example of the exploitation of existing geometrical symmetry for a 4×2 array of identical antenna elements. Left: Array and antenna indexing. Right: Colormap depicting identical sub-blocks $\mathbf{Z}_{i,j}$ in the upper-triangular part of $\mathbf{Z}$.

the C programming language using the Intel MKL library [102]. The simulations were run on an Intel(R) Core(TM) i7-4770 CPU @ 3.4 GHz with 32 GB RAM. In comparison, the 40×4 array (using the exact same geometrical model and meshing) takes 16 min 48 s to simulate on the same computer using the MLFMM solver of the commercial software FEKO [103].

5 Conclusions

The work contained in this thesis has focused on several aspects of mm-wave imaging and phased array technology, in the context of their applicabilities in the aerospace and defense and telecommunication industries. As such, there have been several goals of the presented research which is a result of the various projects in which the performed tasks have been conducted within the framework of. The general conclusions of this work is thus best displayed as summaries of the contributions of the respective papers, in the broader context of their mutual connections to phased arrays, mm-wave frequencies, and imaging.

Numerical Aspects of Phased Arrays for Aerospace Applications

The state-of-the-art CEM tools are continuously evolving to meet demands on improved accuracy and computational efficiency, as well as to realize functionality in EM problems of expanding complexity. Papers I and II deal with two established hybrid MoM techniques—the MBF method and the ACA—as applied to the specific problem of simulating electrically very large antenna arrays under the extreme EM condition of operating them in endfire mode. Such large array configurations are extensively utilized in the aerospace and defense industry as to realize the high gain required of AESA systems, and the antenna elements themselves often incorporate a high level of detail and material complexity resulting in an exceedingly large number of unknowns. A considerable amount of time was dedicated to investigate and implement the selected hybrid MoM techniques as add-ons to an existing in-house MoM-code. More intricate versions of these algorithms were subsequently implemented in the commercial simulation software ESI CEM One.

Paper I presents a comparison study of two previously published algorithms to address electrical interconnections using the MBF method presented in Section 4.4. Very strong coupling between the antenna elements is occurrent in endfire mode operation, since the energy is launched or received along the axis of the array. Since the antennas are interconnected, this is in turn expected to be a source of increased numerical error. The two methods were thus studied and compared under this condition, and it was found that the methods differed in the required number of MBFs for a given numerical accuracy. It should however be stated that both methods were successfully employed on the target problem.

In Paper II, the complete simulation framework presented in Section 4 was utilized to address the issue of bad overall matching of large endfire antenna arrays. This is a well-known consequence of the previously mentioned strong mutual coupling occurring under this excitation condition. The considered geometry was a 200×12 array of bowtie antennas with 643 RWGs per element. Accordingly, the complete simulation volume consisted of more than $1.5 \cdot 10^6$ number of unknowns, thus constituting an EM problem that is infeasible to solve unless a hybrid solver is adapted. By combining the ACA, the MBF method and the block Toeplitz symmetry pre-processing scheme, the 2 400 EEPs and the $2\,400 \times 2\,400$ scattering matrix could be computed at each frequency point in an overall simulation time varying between 8 min 30 s and 27 min 20 s (the difference is due to the number of MBFs being frequency dependent). These were then used in post process to conduct the convex optimization synthesis. The matching problem was formulated as a convex optimization problem, and it was shown that the matching can be significantly improved compared to standard feeding approaches by utilizing the optimized excitation coefficients. Furthermore, the results also suggested that—due to the configuration of the excitation coefficients—it suffices to only let a fraction of the array be active under the endfire operation as the back end contributes very little to the total radiated power.

Phased Arrays for 5G Applications

One of the most emerging technologies (that arguably also should be considered a prerequisite) for potentially realizing mm-wave 5G wireless networks, is that of utilizing phased arrays for the UEs. The topic has been the target of very extensive research the last five years, and has undoubtedly not gone unnoticed among the majority of researchers in the EM community. Accordingly, it is of paramount interest to investigate the capabilities as well as the limitations of such systems when integrated in the UE platform.

Paper III contains the earliest published material (accepted in July 2015) included in this thesis, and presents a conceptual study on the beam steering capabilities of different array configurations composed of two different microstrip antenna designs. Noticeably, the target frequency was chosen as 15 GHz, which is outside of the so-called mm-wave frequency range as the corresponding wavelength is 20 mm. Nevertheless, the concept is still applicable, although the semantic reader may object to the frequent use of the term "mm-wave". The main contribution of the paper is the introduction of two evaluation metrics; the total scan pattern and the coverage efficiency as disclosed in Section 2.5. These metrics were then used to evaluate the performance of the various array configurations when integrated in a mobile phone mock-up.

In Paper IV, the imaging system described in Section 3 was used to run EMF exposure compliance testing of mm-wave 5G cellular handsets. The study comprises results for a 4×1 array configuration operating at 28 GHz that was integrated in a mobile phone mock-up identical to the one disclosed in Paper III. Moreover, the array composed of one of the previously mentioned microstrip antenna designs; although re-designed for operation at 28 GHz instead of at 15 GHz. Results for a 60 GHz corporate-fed 4×4 microstrip patch array—as well as for the benchmarking case of a 60 GHz standard gain horn antenna—are also included. Apart from the presented measurement results, the key novelty of the work is the introduced technique that utilizes a single reference measurement of a small aperture to perform the probe correction. Using this approach, a very accurate spatial alignment of the AUT, with respect to the planar surfaces on which the power density is evaluated on, is obtained. Consequently, large errors in amplitude and phase can be avoided, despite the facts that the planar evaluation surface is situated in the immediate vicinity of the AUT and that the operating wavelength is on a mm-scale. A conference abstract based on this paper was awarded third place out of 19 submissions in the Student Paper Award at the Antenna Measurement Techniques Association (AMTA) 2018 Conference held in Williamsburg, VA.

Millimeter Wave Imaging of Aerospace Composite Panels

As a fundamental part in the production chain of composite structures, EM non-destructive testing (NDT) plays an integral role in the aerospace industry where such structures are utilized to a wide extent. One technique for conducting EM

NDT of composite structures is mm-wave imaging which offers high resolution due to the inherently short wavelengths.

Paper V presents a complete mm-wave imaging system that was developed for the specific purpose of conducting EM NDT of planar composite structures, *i.e.*, composite panels. The system bears close resemblance to the one utilized in Paper IV; conducting a planar near field scan to retrieve the data and utilizing MoM-based processing algorithms to obtain the final image. In addition, an L_1-minimization formulation is presented that exploits the sparsity of the sought-after solution to improve the image quality. The imaging system is transmission-based, *i.e.*, a DUT is illuminated by a transmitting antenna from one side, and on the other side of the DUT a receiving probe registers the transmitted signal across a measurement surface realized by the planar scan. All measurements were conducted in the 60 GHz band, and the measured DUT was an industrially manufactured composite panel. The main novelty presented in this work is related to one of the processing algorithms of the imaging systems. The algorithm permits the image to be retrieved using only a single measurement, which stands in stark contrast to conventional processing algorithms used in similar imaging systems that are reliant on a reference measurement where no DUT is present.

In Paper VI, the previously introduced transmission-based imaging system is further developed and formulated as a reflection-based imaging system instead. Many aircraft structural components contain sheets of RF-impenetrable material, making it unfeasible to conduct transmission-based testing of such DUTs. The hardware component of the imaging system was thus altered and further developed accordingly, to treat planar DUTs mounted on top of a ground plane that emulates or extends the underlying conducting layer. As before, the final image requires only a single measurement to be conducted. A filtering technique was demonstrated and added as a supplemental software component, whereas the rest of the processing algorithms was preserved but altered in accordance to the new experimental setup. A conference abstract based on this paper was rewarded first place out of 19 submissions in the Student Paper Award at the Antenna Measurement Techniques Association (AMTA) 2018 Conference held in Williamsburg, VA.

5.1 Research Outlook and Future Work

There are several potential proceedings—concerning both continued research and future industrial challenges—to the work presented in this thesis. This section provides a brief overview of the most considerable ones.

The two acceleration techniques, the MBF method and the ACA, that are utilized to obtain a fast hybrid MoM-code have the substantial benefit of being kernel-independent. The conducted analysis in Papers I and II are restricted to metallic structures merely due to the existing kernel in the in-house code. Accordingly, the analysis could be extended to treat dielectrics and 3D geometries with interconnections given a more elaborate kernel based on the combined field

integral equation (CFIE). The hybrid MoM-code could further be used to address antenna problems related to massive MIMO systems, due to the code's noniterative characteristic and capability of rapidly calculating the EEPs of large scale multi-port systems.

The usage of mm-wave phased arrays in future 5G devices—the topic of Paper III—is still subject to considerable industrial challenges. The antenna elements should cover a wide impedance bandwidth, preferably enable dual-polarized operation, and sustain a reliable radiation pattern across the whole band. Multiple array configurations are likely required for omnidirectional coverage, and these need to co-exist on a limited form factor with cellular antennas operating at the conventional frequency bands below 6 GHz. Issues related to antenna packaging should be addressed as well, since active components may very well be integrated with the radiating elements to reduce losses in the RF chain. Regarding the topic of EMF exposure for mm-wave 5G devices (addressed in Paper IV), a common consensus on safety limits and standards is yet to be reached between the existing commissions; eliminating the existing inconsistencies may play a significant role in avoiding potential negative influences on the performance and cost of future mobile communication systems.

There is also room for improvement of both the hardware and software components of the imaging systems presented in Papers V and VI. For instance, the measurement time could be reduced by exploiting an array of probes instead of performing a full two-dimensional raster scan using only one probe. This would apply to the experimental setup for the EMF exposure measurement as well. The imaging algorithms presented in Papers V and VI are based on a single frequency problem formulation and could be modified to better exploit the measurement data; acquired over the full frequency bandwidth. A sparser spatial sampling could then potentially be employed if data from multiple discrete frequency points could be utilized simultaneously in the algorithms, implying an additional reduction in measurement time.

Another interesting continuation is to adapt the reflection-based imaging system (presented in Paper VI) for singly curved surfaces or similar shapes that are often exploited in aircraft structural components. This is by no means a straightforward adaptation, and would require, *e.g.*, further studies in how to properly illuminate the DUT, and how to modify the shape and size of the measurement surface. The translational symmetries that are present in the planar measurement scenario would also be compromised, resulting in slower imaging algorithms. With the ever increasing power and speed of computers however, it is unclear whether or not this would constitute a computational bottleneck.

Appendix A ACA Algorithm

The adaptive cross approximation (ACA) algorithm aims to produce a low-rank approximation $\widetilde{\mathbf{Z}}$ to a matrix $\mathbf{Z} \in \mathbb{C}^{N\times M}$, where only a few elements of $\mathbf{Z}$ need to be calculated. The following description is almost verbatim from [87].

The low-rank approximation is a sum of r dyadic products,

$$\widetilde{\mathbf{Z}} = \mathbf{CR} = \sum_{i=1}^{r} \boldsymbol{c}_i \boldsymbol{r}_i \,, \tag{A.1}$$

where $\mathbf{C} \in \mathbb{C}^{N\times r}$ and $\mathbf{R} \in \mathbb{C}^{r\times M}$. Furthermore, the $N \times 1$ column vector $\boldsymbol{c}_i$ is the i:th column of $\mathbf{C}$, and the $1 \times M$ row vector $\boldsymbol{r}_i$ is the i:th row of $\mathbf{R}$. The purpose of the ACA is to achieve, for a given tolerance ϵ,

$$\|\mathbf{P}\|_{\mathrm{F}} = \|\mathbf{Z} - \widetilde{\mathbf{Z}}\|_{\mathrm{F}} \leq \epsilon \|\mathbf{Z}\|_{\mathrm{F}} \,, \tag{A.2}$$

where $\mathbf{P}$ is defined as the error matrix and $\|\cdot\|_{\mathrm{F}}$ denotes the Frobenius norm [93]. Similarly, the L_2-norm is denoted $\|\cdot\|_2$ in the following description. Let $\mathbf{I} = [I_1, I_2, \ldots, I_r]$ and $\mathbf{J} = [J_1, J_2, \ldots, J_r]$ be the arrays containing orderly selected row and column indices of the matrix $\mathbf{Z}$. Using a Matlab notation, $\widetilde{\mathbf{P}}(I_1, :)$ stands for the I_1:th row of the matrix $\widetilde{\mathbf{P}}$. At the n:th iteration, the matrix $\widetilde{\mathbf{Z}}$ is $\widetilde{\mathbf{Z}}^{(n)}$. The following step-by-step procedure describes the algorithm:

Initialization:

1. Initialize the 1:st row index $I_1 = 1$ and set $\widetilde{\mathbf{Z}} = 0$.
2. Initialize the 1:st row of the approximate error matrix: $\widetilde{\mathbf{P}}(I_1, :) = \mathbf{Z}(I_1, :)$.
3. Find the 1:st column index J_1: $|\widetilde{\mathbf{P}}(I_1, J_1)| = \max_j\{\, |\widetilde{\mathbf{P}}(I_1, j)| \,\}$.
4. $\boldsymbol{r}_1 = \widetilde{\mathbf{P}}(I_1, :)/\widetilde{\mathbf{P}}(I_1, J_1)$.
5. Initialize the 1:st column of $\widetilde{\mathbf{P}}$: $\widetilde{\mathbf{P}}(:, J_1) = \mathbf{Z}(:, J_1)$.
6. $\boldsymbol{c}_1 = \widetilde{\mathbf{P}}(:, J_1)$.
7. $\|\widetilde{\mathbf{Z}}^{(1)}\|_{\mathrm{F}}^2 = \|\widetilde{\mathbf{Z}}^{(0)}\|_{\mathrm{F}}^2 + \|\boldsymbol{c}_1\|_2^2 \|\boldsymbol{r}_1\|_2^2$.
8. Find 2:nd row index I_2: $|\widetilde{\mathbf{P}}(I_2, J_1)| = \max_i\{\, |\widetilde{\mathbf{P}}(i, J_1)| \,\}$, $i \neq I_1$.

***n*:th iteration:**

1. Update I_n:th row of $\widetilde{\mathbf{P}}$: $\widetilde{\mathbf{P}}(I_n, :) = \mathbf{Z}(I_n, :) - \sum_{l=1}^{n-1} \boldsymbol{c}_l(I_n)\boldsymbol{r}_l$.
2. Find n:th column index J_n: $|\widetilde{\mathbf{P}}(I_n, J_n)| = \max_j\{\, |\widetilde{\mathbf{P}}(I_n, j)| \,\}$, $j \neq J_1, J_2, \ldots, J_{n-1}$.
3. $\boldsymbol{r}_n = \widetilde{\mathbf{P}}(I_n, :)/\widetilde{\mathbf{P}}(I_n, J_n)$.

4. Update J_n:th column $\widetilde{\mathbf{P}}$: $\widetilde{\mathbf{P}}(:, J_n) = \mathbf{Z}(:, J_n) - \sum_{l=1}^{n-1} \boldsymbol{r}_l(J_n)\boldsymbol{c}_l$.
5. $\boldsymbol{c}_n = \widetilde{\mathbf{P}}(:, J_n)$.
6. $\|\widetilde{\mathbf{Z}}^{(n)}\|_{\mathrm{F}}^2 = \|\widetilde{\mathbf{Z}}^{(n-1)}\|_{\mathrm{F}}^2 - 2\sum_{j=1}^{n-1}\left(|\boldsymbol{c}_j^{\mathrm{T}}\boldsymbol{c}_n| \cdot |\boldsymbol{r}_j^{\mathrm{T}}\boldsymbol{r}_n|\right) + \|\boldsymbol{c}_n\|_2^2\|\boldsymbol{r}_n\|_2^2$.
7. Check convergence: If $\|\boldsymbol{c}_n\|_2\|\boldsymbol{r}_n\|_2 \leq \epsilon\|\widetilde{\mathbf{Z}}^{(n)}\|_{\mathrm{F}}$, end iteration.
8. Find next row index I_{n+1}: $|\widetilde{\mathbf{P}}(I_{n+1}, J_n)| = \max_i\{\,|\widetilde{\mathbf{P}}(i, J_n)\,|\}$, $i \neq I_1, I_2, \ldots, I_n$.

The ACA algorithm thus requires computation of r rows and columns of $\mathbf{Z}$. For computation of a single matrix $N \times M$ matrix, memory storage and computational complexity scales as $\mathcal{O}(r(N+M))$ and $\mathcal{O}(r^2(N+M))$, respectively.

References

[1] R. C. Hansen, *Phased array antennas*. John Wiley & Sons, 2009, vol. 213.

[2] H. van Bezouwen, H.-P. Feldle, and W. Holpp, "Status and trends in AESA-based radar," in *MTT-S International Microwave Symposium*. IEEE, 2010, pp. 526–529.

[3] A. Kinghorn, "Where next for airborne AESA technology?" *IEEE Aerosp. Electron. Syst. Mag.*, vol. 24, no. 11, pp. 16–21, 2009.

[4] "ESI Group CEM One Solution," https://www.esi-group.com/software-solutions/virtual-environment/electromagnetics/cem-one-solution, accessed December, 2018.

[5] J. Wells, "Faster than fiber: the future of multi-Gb/s wireless," *IEEE Microw. Mag.*, vol. 10, no. 3, pp. 104–112, Mar. 2009.

[6] T. S. Rappaport, S. Sun, R. Mayzus, H. Zhao, Y. Azar, K. Wang, G. N. Wong, J. K. Schulz, M. Samimi, and F. Gutierrez, "Millimeter wave mobile communications for 5G cellular: It will work!" *Access, IEEE*, vol. 1, pp. 335–349, 2013.

[7] F. Boccardi, R. W. Heath, A. Lozano, T. L. Marzetta, and P. Popovski, "Five disruptive technology directions for 5G," *IEEE Commun. Mag.*, vol. 52, no. 2, pp. 74–80, 2014.

[8] B. Xu, Z. Ying, L. Scialacqua, A. Scannavini, L. J. Foged, T. Bolin, K. Zhao, S. He, and M. Gustafsson, "Radiation performance analysis of 28 GHz antennas integrated in 5G mobile terminal housing," *IEEE Access*, vol. 6, pp. 48 088–48 101, 2018.

[9] W. Roh, J.-Y. Seol, J. Park, B. Lee, J. Lee, Y. Kim, J. Cho, K. Cheun, and F. Aryanfar, "Millimeter-wave beamforming as an enabling technology for 5G cellular communications: Theoretical feasibility and prototype results," *IEEE Commun. Mag*, vol. 52, no. 2, pp. 106–113, 2014.

[10] W. Hong, K. Baek, Y. G. Kim, Y. Lee, and B. Kim, "mmWave phased-array with hemispheric coverage for 5th generation cellular handsets," in *European Conf. on Antennas and Propagation (EuCAP)*. IEEE, 2014, pp. 714–716.

[11] H. Zhao, R. Mayzus, S. Sun, M. Samimi, J. K. Schulz, Y. Azar, K. Wang, G. N. Wong, F. Gutierrez, and T. S. Rappaport, "28 GHz millimeter wave cellular communication measurements for reflection and penetration loss in and around buildings in New York City," in *IEEE Int. Conference on Communications (ICC)*. IEEE, 2013, pp. 5163–5167.

[12] Y. Azar, G. N. Wong, K. Wang, R. Mayzus, J. K. Schulz, H. Zhao, F. Gutierrez, D. Hwang, and T. S. Rappaport, "28 GHz propagation measurements for outdoor cellular communications using steerable beam antennas in new york city," in *IEEE Int. Conf. on Communications (ICC)*. IEEE, 2013, pp. 5143–5147.

[13] S. Han, I. Chih-Lin, Z. Xu, and C. Rowell, "Large-scale antenna systems with hybrid analog and digital beamforming for millimeter wave 5G," *IEEE Commun. Mag*, vol. 53, no. 1, pp. 186–194, 2015.

[14] J. G. Andrews, S. Buzzi, W. Choi, S. V. Hanly, A. Lozano, A. C. Soong, and J. C. Zhang, "What will 5G be?" *IEEE J. Sel. Areas Commun.*, vol. 32, no. 6, pp. 1065–1082, 2014.

[15] W. Hong, K.-H. Baek, Y. Lee, Y. Kim, and S.-T. Ko, "Study and prototyping of practically large-scale mmwave antenna systems for 5G cellular devices," *IEEE Commun. Mag*, vol. 52, no. 9, pp. 63–69, 2014.

[16] B. Xu, K. Zhao, B. Thors, D. Colombi, O. Lundberg, Z. Ying, and S. He, "Power density measurements at 15 GHz for RF EMF compliance assessments of 5G user equipment," *IEEE Trans. Antennas Propag.*, vol. 65, no. 12, pp. 6584–6595, 2017.

[17] K. Zhao, J. Helander, D. Sjöberg, S. He, T. Bolin, and Z. Ying, "User body effect on phased array in user equipment for 5G mmWave communication system," *IEEE Antennas Wireless Propag. Lett.*, vol. 16, no. 1, pp. 864–867, 2016.

[18] T. Bai and R. W. Heath, "Coverage and rate analysis for millimeter-wave cellular networks," *IEEE Trans. Wirel. Commun.*, vol. 14, no. 2, pp. 1100–1114, 2015.

[19] K. Zhao, "Mobile antenna systems for 4G and 5G applications with user body interaction," Doctoral thesis, KTH Royal Institute of Technology, School of Electrical Engineering, SE-100 44 Stockholm, Sweden, 2017, http://www.kth.se.

[20] S. S. Ahmed, A. Schiessl, F. Gumbmann, M. Tiebout, S. Methfessel, and L.-P. Schmidt, "Advanced microwave imaging," *IEEE Microw. Mag.*, vol. 13, no. 6, pp. 26–43, 2012.

[21] S. Kharkovsky and R. Zoughi, "Microwave and millimeter wave nondestructive testing and evaluation - overview and recent advances," *IEEE Instrum. Meas. Mag.*, vol. 10, no. 2, pp. 26–38, 2007.

[22] K. Persson, M. Gustafsson, G. Kristensson, and B. Widenberg, "Radome diagnostics — source reconstruction of phase objects with an equivalent currents approach," *IEEE Trans. Antennas Propag.*, vol. 62, no. 4, 2014.

[23] J. T. Case, S. Kharkovsky, R. Zoughi, G. Steffes, F. L. Hepburn, D. O. Thompson, and D. E. Chimenti, "Millimeter wave holographical inspection of honeycomb composites," in *AIP Conference Proceedings*, vol. 975, no. 1. AIP, 2008, pp. 970–975.

[24] R. B. Deo, J. H. Starnes, and R. C. Holzwarth, "Low-cost composite materials and structures for aircraft applications," in *RTO AVT Specialists' Meeting on "Low Cost Composite Structures"*, 2001.

[25] W. D. Callister, D. G. Rethwisch *et al.*, *Materials science and engineering: an introduction*. New York: John Wiley & Sons, 2007, vol. 7.

[26] I. M. Daniel, O. Ishai, I. M. Daniel, and I. Daniel, *Engineering mechanics of composite materials*. New York: Oxford University Press, 1994, vol. 3.

[27] D. Tayli, "Computational tools for antenna analysis and design," Doctoral thesis, Lund University, Department of Electrical and Information Technology, P.O. Box 118, S-221 00 Lund, Sweden, 2018, http://www.eit.lth.se.

[28] C. A. Balanis, *Antenna Theory*, 3rd ed. Hoboken, NJ: John Wiley & Sons, 2005.

[29] E. G. Larsson, O. Edfors, F. Tufvesson, and T. L. Marzetta, "Massive MIMO for next generation wireless systems," *IEEE Commun. Mag*, vol. 52, no. 2, pp. 186–195, 2014.

[30] S. Sun, T. S. Rappaport, R. W. Heath, A. Nix, and S. Rangan, "MIMO for millimeter-wave wireless communications: Beamforming, spatial multiplexing, or both?" *IEEE Commun. Mag*, vol. 52, no. 12, pp. 110–121, 2014.

[31] M. A. Richards, J. Scheer, W. A. Holm, and W. L. Melvin, *Principles of modern radar*. SciTech Publishing Inc., 2010.

[32] H. T. Friis, "A note on a simple transmission formula," *Proc. IRE*, vol. 34, no. 5, pp. 254–256, 1946.

[33] IEEE145-2013, *IEEE Standard Definition of Terms for Antennas*, Antenna Standards Committee of the IEEE Antennas and Propagation Society, December 1993.

[34] S. J. Orfanidis, "Electromagnetic Waves and Antennas," 2014, available online at http://www.ece.rutgers.edu/ orfanidi/ewa/.

[35] R. W. P. King and S. S. Sandler, "The theory of endfire arrays," *IEEE Trans. Antennas Propag.*, vol. 12, no. 3, pp. 276–280, 1964.

[36] W. W. Hansen and J. R. Woodyard, "A new principle in directional antenna design," *Proc. IRE*, vol. 26, no. 3, pp. 333–345, 1938.

[37] C. L. Dolph, "A current distribution for broadside arrays which optimizes the relationship between beam width and side-lobe level," *Proc. IRE*, vol. 34, no. 6, pp. 335–348, 1946.

[38] E. C. Dufort, "Pattern synthesis based on adaptive array theory," *IEEE Trans. Antennas Propag.*, vol. 37, no. 8, pp. 1011–1018, 1989.

[39] Y. Lo, S. Lee, and Q. Lee, "Optimization of directivity and signal-to-noise ratio of an arbitrary antenna array," *IEE Proceedings*, vol. 54, no. 8, pp. 1033–1045, 1966.

[40] H. Lebret and S. Boyd, "Antenna array pattern synthesis via convex optimization," *IEEE Trans. Signal Process.*, vol. 45, no. 3, pp. 526–532, 1997.

[41] A. B. Gershman, N. D. Sidiropoulos, S. Shahbazpanahi, M. Bengtsson, and B. Ottersten, "Convex optimization-based beamforming," *IEEE Signal Process. Mag.*, vol. 27, no. 3, pp. 62–75, 2010.

[42] H. Van Bui, S. N. Jha, and C. Craeye, "Fast full-wave synthesis of printed antenna arrays including mutual coupling," *IEEE Trans. Antennas Propag.*, vol. 64, no. 12, pp. 5163–5171, 2016.

[43] T. Zhang and W. Ser, "Robust beampattern synthesis for antenna arrays with mutual coupling effect," *IEEE Trans. Antennas Propag.*, vol. 59, no. 8, pp. 2889–2895, 2011.

[44] S. E. Nai, W. Ser, Z. L. Yu, and H. Chen, "Beampattern synthesis for linear and planar arrays with antenna selection by convex optimization," *IEEE Trans. Antennas Propag.*, vol. 58, no. 12, pp. 3923–3930, 2010.

[45] M. G. Bray, D. H. Werner, D. W. Boeringer, and D. W. Machuga, "Optimization of thinned aperiodic linear phased arrays using genetic algorithms to reduce grating lobes during scanning," *IEEE Trans. Antennas Propag.*, vol. 50, no. 12, pp. 1732–1742, 2002.

[46] G. Holtrup, A. Marguinaud, and J. Citerne, "Synthesis of electronically steerable antenna arrays with elements on concentric rings with reduced sidelobes," in *Antennas and Propagation Society International Symposium, 2001 IEEE*, vol. 3. IEEE, 2001, pp. 800–803.

[47] D. M. Pozar, *Microwave Engineering*, 3rd ed. New York, NY: John Wiley & Sons, 2005.

[48] O. Wing, *Classical Circuit Theory.* New York: Springer, 2008.

[49] M. Manteghi and Y. Rahmat-Samii, "Multiport characteristics of a wideband cavity backed annular patch antenna for multipolarization operations," *IEEE Trans. Antennas Propag.*, vol. 53, no. 1, pp. 466–474, 2005.

[50] L. Lu, G. Y. Li, A. L. Swindlehurst, A. Ashikhmin, and R. Zhang, "An overview of massive MIMO: Benefits and challenges," *IEEE J. Sel. Topics Signal Process.*, vol. 8, no. 5, pp. 742–758, 2014.

[51] M. Jankiraman, *Space-time codes and MIMO systems.* Artech House, 2004.

[52] A. Paulraj, R. Nabar, and D. Gore, *Introduction to Space-Time Wireless Communications.* Cambridge: Cambridge University Press, 2003.

[53] The International Commission on Non-Ionizing Radiation Protection, "Guidelines for limiting exposure to time-varying electric, magnetic, and electromagnetic fields (up to 300 GHz)," *Health Phys.*, vol. 74, no. 4, pp. 494–521, April 1998.

[54] *IEEE Standard for Safety Levels with Respect to Human Exposure to Radio Frequency Electromagnetic Fields, 3kHz to 300 GHz*, IEEE Standard C95.1-2005 (Revision of IEEE Standard C95.1-1991), December 2006.

[55] *FCC, Code of Federal Regulations CFR Title 47, Part 1.1310, Radiofrequency Radiation Exposure Limits*, Federal Commun. Commission, Washington DC, USA, August 1997.

[56] "NTT Docomo, Docomo 5G white paper," https://www.nttdocomo.co.jp/english/corporate/technology/whitepaper_5g/, accessed July, 2014.

[57] D. Colombi, B. Thors, and C. Törnevik, "Implications of EMF exposure limits on output power levels for 5G devices above 6 GHz," *IEEE Antennas Wireless Propag. Lett.*, vol. 14, pp. 1247–1249, 2015.

[58] K. Zhao, Z. Ying, and S. He, "EMF exposure study concerning mmwave phased array in mobile devices for 5G communication," *IEEE Antennas Wireless Propag. Lett.*, vol. 15, pp. 1132–1135, 2016.

[59] A. D. Yaghjian, "An overview of near-field antenna measurements," *IEEE Trans. Antennas Propag.*, vol. 34, no. 1, pp. 30–45, 1986.

[60] M. A. Abou-Khousa, A. Ryley, S. Kharkovsky, R. Zoughi, D. Daniels, N. Kreitinger, G. Steffes, D. O. Thompson, and D. E. Chimenti, "Comparison of X-ray, millimeter wave, shearography and through-transmission ultrasonic methods for inspection of honeycomb composites," in *AIP Conference Proceedings*, vol. 894, no. 1, 2007, pp. 999–1006.

[61] K. Persson and M. Gustafsson, "Reconstruction of equivalent currents using a near-field data transformation – with radome applications," *Prog. Electromagn. Res.*, vol. 54, pp. 179–198, 2005.

[62] K. Persson, M. Gustafsson, and G. Kristensson, "Reconstruction and visualization of equivalent currents on a radome using an integral representation formulation," *Progress In Electromagnetics Research*, vol. 20, pp. 65–90, 2010.

[63] "Thorlabs," https://www.thorlabs.com/navigation.cfm?guide_id=2174, accessed: 2018-12-03.

[64] S. M. Rao, *Time Domain Electromagnetics*. Academic Press, 1999.

[65] R. J. I. Marks, *Introduction to Shannon sampling and interpolation theory*. Springer Science & Business Media, 2012.

[66] A. D. Yaghjian, "Approximate formulas for the far field and gain of open-ended rectangular waveguide," *IEEE Trans. Antennas Propag.*, vol. 32, no. 4, pp. 378–384, 1984.

[67] T. Laitinen, S. Pivnenko, and O. Breinbjerg, "Iterative probe correction technique for spherical near-field antenna measurements," *IEEE Antennas and Wireless Propagation Letters*, vol. 4, pp. 221–223, 2005.

[68] O. Bucci and T. Isernia, "Electromagnetic inverse scattering: Retrievable information and measurement strategies," *Radio Sci.*, vol. 32, no. 6, pp. 2123–2137, 1997.

[69] G. Kristensson, *Scattering of Electromagnetic Waves by Obstacles*. Edison, NJ: SciTech Publishing, an imprint of the IET, 2016.

[70] P. C. Hansen, *Discrete inverse problems: insight and algorithms*. Society for Industrial & Applied Mathematics, 2010, vol. 7.

[71] L. Poli, G. Oliveri, and A. Massa, "Microwave imaging within the first-order Born approximation by means of the contrast-field Bayesian compressive sensing," *IEEE Trans. Antennas Propag.*, vol. 60, no. 6, pp. 2865–2879, 2012.

[72] A. Devaney, "Inverse-scattering theory within the Rytov approximation," *Opt. Lett.*, vol. 6, no. 8, pp. 374–376, 1981.

[73] P. M. van den Berg and R. E. Kleinman, "A contrast source inversion method," *Inverse Problems*, vol. 13, pp. 1607–1620, 1997.

[74] A. Massa, P. Rocca, and G. Oliveri, "Compressive sensing in electromagnetics-a review," *IEEE Antennas Propag. Mag.*, vol. 57, no. 1, pp. 224–238, 2015.

[75] E. J. Candès and M. B. Wakin, "An introduction to compressive sampling," *IEEE Signal Process. Mag.*, vol. 25, no. 2, pp. 21–30, 2008.

[76] G. Oliveri and A. Massa, "Bayesian compressive sampling for pattern synthesis with maximally sparse non-uniform linear arrays," *IEEE Trans. Antennas Propag.*, vol. 59, no. 2, pp. 467–481, 2011.

[77] M. D. Migliore, "A compressed sensing approach for array diagnosis from a small set of near-field measurements," *IEEE Trans. Antennas Propag.*, vol. 59, no. 6, pp. 2127–2133, 2011.

[78] G. Oliveri, M. Salucci, N. Anselmi, and A. Massa, "Compressive sensing as applied to inverse problems for imaging: Theory, applications, current trends, and open challenges," *IEEE Antennas Propag. Mag.*, vol. 59, no. 5, pp. 34–46, 2017.

[79] L. Guo and A. M. Abbosh, "Microwave imaging of nonsparse domains using Born iterative method with wavelet transform and block sparse Bayesian learning," *IEEE Trans. Antennas Propag.*, vol. 63, no. 11, pp. 4877–4888, 2015.

[80] G. H. Golub and C. F. van Loan, *Matrix Computations*. Baltimore, MD: The Johns Hopkins University Press, 1983.

[81] M. Gustafsson, M. Sebesta, B. Bengtsson, S.-G. Pettersson, P. Egelberg, and T. Lenart, "High resolution digital transmission microscopy—a Fourier holography approach," *Optics and Lasers in Engineering*, vol. 41, no. 3, pp. 553–563, 2004.

[82] W. C. Chew, M. S. Tong, and B. Hu, *Integral Equation Methods for Electromagnetic and Elastic Waves*. Morgan & Claypool, 2008, vol. 12.

[83] D. B. Davidson, *Computational Electromagnetics for RF and Microwave Engineering*. Cambridge University Press, 2005.

[84] J. M. Jin, *Theory and Computation of Electromagnetic Fields*. Wiley, 2011.

[85] L. V. Kantorovich, *Approximate methods of higher analysis*. Noordhoff, 1958.

[86] S. M. Rao, D. R. Wilton, and A. W. Glisson, "Electromagnetic scattering by surfaces of arbitrary shape," *IEEE Trans. Antennas Propag.*, vol. 30, no. 3, pp. 409–418, 1982.

[87] K. Zhao, M. N. Vouvakis, and J.-F. Lee, "The adaptive cross approximation algorithm for accelerated method of moments computations of EMC problems," *IEEE Trans. Electromagn. Compat.*, vol. 47, no. 4, pp. 763–773, 2005.

[88] M. Bebendorf, "Approximation of boundary element matrices," *Numerische Mathematik*, vol. 86, no. 4, pp. 565–589, 2000.

[89] S. Kurz, O. Rain, and S. Rjasanow, "The adaptive cross-approximation technique for the 3d boundary-element method," *IEEE Trans. Magnetics*, vol. 38, no. 2, pp. 421–424, 2002.

[90] A. Heldring, E. Ubeda, and J. Rius, "Stochastic estimation of the frobenius norm in the aca convergence criterion," *IEEE Trans. Antennas Propag.*, vol. 63, no. 3, pp. 1155–1158, 2015.

[91] X. Chen, C. Gu, J. Ding, Z. Li, and Z. Niu, "Multilevel fast adaptive cross-approximation algorithm with characteristic basis functions," *IEEE Trans. Antennas Propag.*, vol. 63, no. 9, pp. 3994–4002, 2015.

[92] R. Maaskant, R. Mittra, and A. Tijhuis, "Fast analysis of large antenna arrays using the characteristic basis function method and the adaptive cross approximation algorithm," *IEEE Trans. Antennas Propag.*, vol. 56, no. 11, pp. 3440–3451, 2008.

[93] G. H. Golub and C. F. van Loan, *Matrix Computations*, 4th ed. Baltimore, MD: The Johns Hopkins University Press, 2013.

[94] C. Craeye, J. Laviada, R. Maaskant, and R. Mittra, "Macro basis function framework for solving maxwell's equations in surface integral equation form," *The FERMAT Journal*, vol. 3, pp. 1–16, 2014.

[95] L. Matekovits, V. A. Laza, and G. Vecchi, "Analysis of large complex structures with the synthetic-functions approach," *IEEE Trans. Antennas Propag.*, vol. 55, no. 9, pp. 2509–2521, 2007.

[96] D. J. Bekers, S. J. van Eijndhoven, A. A. van de Ven, P.-P. Borsboom, and A. G. Tijhuis, "Eigencurrent analysis of resonant behavior in finite antenna arrays," *IEEE Trans. Microwave Theory Tech.*, vol. 54, no. 6, pp. 2821–2829, 2006.

[97] E. Garcia, C. Delgado, L. Lozano, I. Gonzalez-Diego, and M. F. Catedra, "An efficient hybrid-scheme combining the characteristic basis function method and the multilevel fast multipole algorithm for solving bistatic RCS and radiation problems," *Progress In Electromagnetics Research B*, vol. 34, pp. 327–343, 2011.

[98] P. De Vita, A. Freni, L. Matekovits, P. Pirinoli, and G. Vecchi, "A combined AIM-SFX approach for large complex arrays," in *Antennas and Propagation Society International Symposium, 2007 IEEE*. IEEE, 2007, pp. 3452–3455.

[99] F. Jensen and A. Frandsen, "On the number of modes in spherical wave expansions," TICRA, TICRA, Læderstræde 34, DK-1201 Copenhagen, Denmark, Tech. Rep., 2009.

[100] S. N. Makarov, *Antenna and EM Modeling with MATLAB*. New York, NY: John Wiley & Sons, 2002.

[101] J. M. Ortega, *Matrix Theory (A Second Course)*. Springer Science & Business Media, 2013.

[102] Intel, "Intel Math Kernel Library," 2007.

[103] S. A. Altair Development S.A. (Pty) Ltd Stellenbosch, "FEKO, Field Computations Involving Bodies of Arbitrary Shape, Suite 7.0," https://www.feko.info/, 2014, accessed November, 2014.